AGU PUBLICATIONS

JGR

Journal of Geophysical Research: Planets

RESEARCH ARTICLE
10.1002/2014JE004686

Key Point:
- Hydrated Mg and Ca sulfate Burns formation minerals mapped with MRO and MER data

Correspondence to:
R. E. Arvidson,
arvidson@wunder.wustl.edu

Citation:
Arvidson, R. E., et al. (2015), Mars Reconnaissance Orbiter and Opportunity observations of the Burns formation: Crater hopping at Meridiani Planum, *J. Geophys. Res. Planets*, *120*, 429–451, doi:10.1002/2014JE004686.

Received 1 JUL 2014
Accepted 4 FEB 2015
Accepted article online 9 FEB 2015
Published online 18 MAR 2015

Mars Reconnaissance Orbiter and Opportunity observations of the Burns formation: Crater hopping at Meridiani Planum

R. E. Arvidson[1], J. F. Bell III[2], J. G. Catalano[1], B. C. Clark[3], V. K. Fox[1], R. Gellert[4], J. P. Grotzinger[5], E. A. Guinness[1], K. E. Herkenhoff[6], A. H. Knoll[7], M. G. A. Lapotre[5], S. M. McLennan[8], D. W. Ming[9], R. V. Morris[9], S. L. Murchie[10], K. E. Powell[1], M. D. Smith[11], S. W. Squyres[12], M. J. Wolff[3], and J. J. Wray[13]

[1]Department of Earth and Planetary Sciences, Washington University in Saint Louis, Missouri, USA, [2]School of Earth and Space Exploration, Arizona State University, Tempe, Arizona, USA, [3]Space Science Institute, Boulder, Colorado, USA, [4]Department of Physics, University of Guelph, Guelph, Ontario, Canada, [5]Division of Geological and Planetary Sciences, California Institute of Technology, Pasadena, California, USA, [6]U.S. Geological Survey, Astrogeology Science Center, Flagstaff, Arizona, USA, [7]Department of Organismic and Evolutionary Biology, Harvard University, Cambridge, Massachusetts, USA, [8]Department of Geosciences, Stony Brook University, Stony Brook, New York, USA, [9]NASA Johnson Space Center, Houston, Texas, USA, [10]Applied Physics Laboratory, Johns Hopkins University, Laurel, Maryland, USA, [11]NASA Goddard Space Flight Center, Greenbelt, Maryland, USA, [12]Department of Astronomy, Cornell University, Ithaca, New York, USA, [13]School of Earth and Atmospheric Sciences, Georgia Institute of Technology, Atlanta, Georgia, USA

Abstract Compact Reconnaissance Imaging Spectrometer for Mars hyperspectral (1.0–2.65 μm) along-track oversampled observations covering Victoria, Santa Maria, Endeavour, and Ada craters were processed to 6 m/pixel and used in combination with Opportunity observations to detect and map hydrated Mg and Ca sulfate minerals in the Burns formation. The strongest spectral absorption features were found to be associated with outcrops that are relatively young and fresh (Ada) or preferentially scoured of dust, soil, and coatings by prevailing winds. At Victoria and Santa Maria, the scoured areas are on the southeastern rims and walls, opposite to the sides where wind-blown sands extend out of the craters. At Endeavour, the deepest absorptions are in Botany Bay, a subdued and buried rim segment that exhibits high thermal inertias, extensive outcrops, and is interpreted to be a region of enhanced wind scour extending up and out of the crater. Ada, Victoria, and Santa Maria outcrops expose the upper portion of the preserved Burns formation and show spectral evidence for the presence of kieserite. In contrast, gypsum is pervasive spectrally in the Botany Bay exposures. Gypsum, a relatively insoluble evaporative mineral, is interpreted to have formed close to the contact with the Noachian crust as rising groundwaters brought brines close to and onto the surface, either as a direct precipitate or during later diagenesis. The presence of kieserite at the top of the section is hypothesized to reflect precipitation from evaporatively concentrated brines or dehydration of polyhydrated sulfates, in both scenarios as the aqueous environment evolved to very arid conditions.

1. Introduction

The Mars Exploration Rover, Opportunity, landed on 24 January 2004 on the Meridiani plains in the ~20 m wide Eagle crater and spent its first 2 months of operations characterizing sulfate-rich sandstones of the Burns formation [*Squyres et al.*, 2004] (Figures 1 and 2). Its next major target was the ~150 m wide Endurance crater, where it spent its first Martian winter characterizing in detail an ~8 m thick stratigraphic section of the Burns formation materials [*Grotzinger et al.*, 2005]. Crater hopping continued, focusing on detailed remote sensing of the ~800 m diameter Victoria crater [*Squyres et al.*, 2009], followed by in situ observations of the Burns formation strata exposed on the northwestern crater walls. Opportunity next focused on the remote sensing of the relatively fresh ~100 m diameter Santa Maria crater and in situ measurements of Burns formation materials exposed on its southeastern rim. The rover then traversed to the Cape York rim segment of the ~22 km wide Noachian age Endeavour crater, where combined orbital and rover data show the presence of smectites in layered rocks that are unconformably overlain by impact breccias [*Arvidson et al.*, 2014].

In this paper we continue to take advantage of combined orbital and in situ observations obtained during crater hopping and include three Mars Reconnaissance Orbiter (MRO) Compact Reconnaissance Imaging

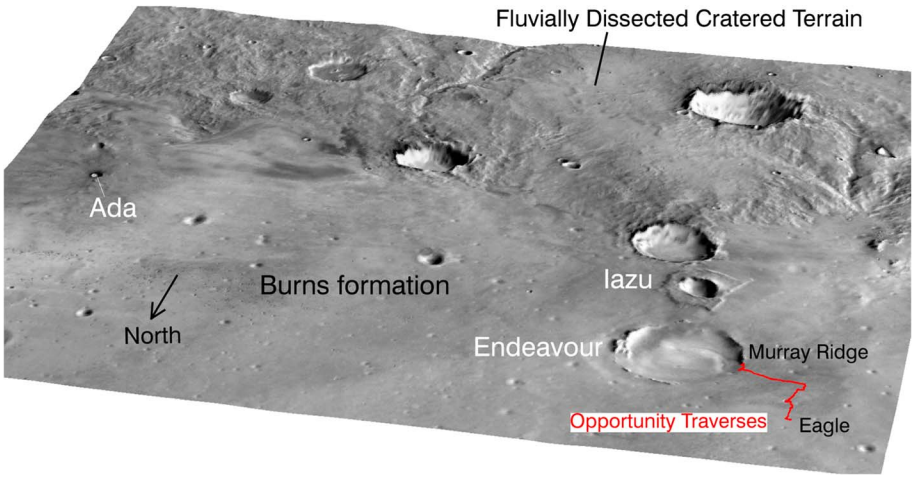

Figure 1. Perspective view looking to the southeast at Meridiani Planum and its contact with the fluvially dissected cratered terrain. Meridiani Planum is underlain by the Burns formation sulfate-rich sandstones that embay the cratered terrain. Opportunity explored and characterized these sandstones from 2004 to 2011, when the rover transitioned onto the Cape York rim segment of the partially buried Noachian Endeavour crater. The Murray Ridge rim segment to the south of Cape York is labeled. Endeavour craters formed before the Burns sandstones were deposited. Ada is a young, ~2.2 km wide crater that exposes the top of the Burns formation strata and is located ~140 km to the east of Endeavour. The red line shows Opportunity's traverses. THEMIS daytime thermal infrared mosaic has been overlain onto a Mars Orbiter Laser Altimeter-based digital elevation map to produce this perspective view.

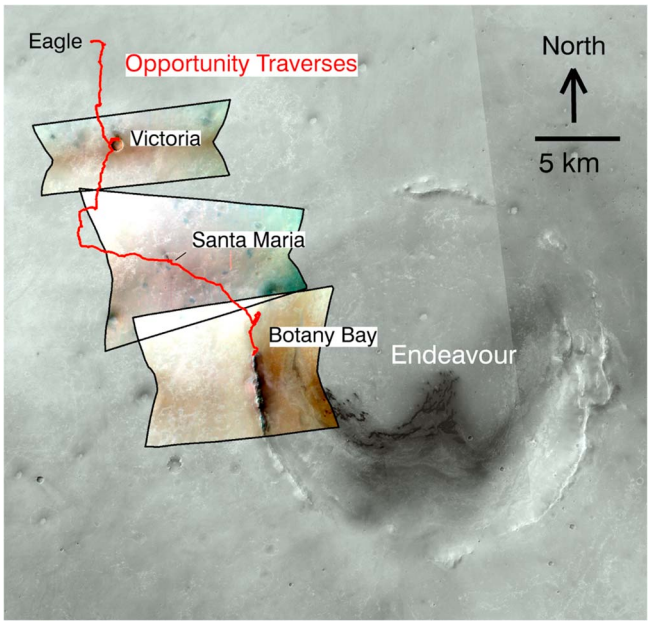

Figure 2. Mars Reconnaissance Orbiter Context Imager-based mosaic overlain with false color infrared CRISM along-track oversampled (ATO) observations covering Opportunity's traverses (red). The CRISM ATO data shown were used to retrieve mineral signatures that were combined with Opportunity's surface observations to understand the nature of Burns formation materials where extensive outcrops are exposed. The dune spectrum shown in Figure 4 was retrieved from a homogeneous dark dune in the southeastern side of the southernmost CRISM scene. (top to bottom) The ATOs are FRT0001C7D2 (Victoria crater), FRT0001B8A4 (Santa Maria crater), and FRT00019E9C (Botany Bay, Endeavour crater). Bands located at 1.08, 1.51, and 2.53 μm are shown as blue, green, and red colors (BGR).

Spectrometer for Mars (CRISM) [*Murchie et al.*, 2007] data sets acquired in an along-track oversampled (ATO) mode (Table 1) [*Fraeman et al.*, 2013; *Arvidson et al.*, 2014] over Victoria, Santa Maria, and Endeavour craters (Figure 2). ATOs provide ~6 m/pixel resolution along track, in contrast to ~18 m/pixel data acquired in the normal full resolution targeted (FRT) mode. MRO High Resolution Imaging Science Experiment (HiRISE) [*McEwen et al.*, 2007] data are also utilized to provide morphologic contexts. An ATO over the ~2.2 km diameter fresh crater, Ada (Figure 1 and Table 1), located ~140 km to the east of Endeavour, is also included because of extensive exposures of Burns formation materials. The combined CRISM and rover-based results are then integrated to provide value-added insight into the deposition and alteration of the sulfate minerals in the Burns formation. The use of the CRISM ATO data was crucial to enabling this focus because the increased spatial resolution allowed us to isolate and identify spectral end-members for what turned out to be relatively small outcrops comparatively free of dust, soil, and coatings.

Table 1. Summary of CRISM Data Sets, Including Observational Parameters[a]

FRT0001FCA1 Ada crater	
Date	20/8/2011
Ls	348°
Sol	2692
τ_{dust} (at 0.90 μm)	1.02
τ_{ice} (at 0.32 μm)	0.10
Pressure	6.72 mb
H_2O ppt	12.9 μm
T detector	−147°C
Delta λ	−0.0251
Delta elevation	0.085 km
Incidence angle	32°
Emergence angle range	8–38°
Phase angle range	40–53°
FRT0001C7D2 Victoria crater visited by Opportunity	
Date	19/12/2010
Ls	202°
Sol	2454
τ_{dust} (at 0.9 μm)	0.70
τ_{ice} (at 0.32 μm)	0.07
Pressure	6.3 mb
H_2O ppt	14.6 μm
T detector	−147°C
Delta λ	0.3558
Delta elevation	0.055 km
Incidence angle	55°
Emergence angle range	1–36°
Phase angle range	55–65°
FRT0001B8A4 Santa Maria crater visited by Opportunity	
Date	25/10/2010
Ls	170°
Sol	2400
τ_{dust} (at 0.9 μm)	0.51
τ_{ice} (at 0.32 μm)	0.11
Pressure	5.84 mb
H_2O ppt	16.5 μm
T detector	−148°C
Delta λ	0.0862
Delta elevation	0.146 km
Incidence angle	56°
Emergence angle range	17–39°
Phase angle range	37–57°
FRT000019E9c Botany Bay visited by Opportunity	
Date	23/7/2010
Ls	123°
Sol	2309
τ_{dust} (at 0.9 μm)	0.20
τ_{ice} (at 0.32 μm)	0.11
Pressure	6.0 mb
H_2O ppt	22 μm
T detector	−148°C
Delta λ	0.0847
Delta elevation	0.341 km

2. Previous Work

The identification and mapping of hydrated sulfates on a regional scale in Meridiani Planum were pioneered by acquisition and analysis of Mars Express Observatoire pour la Minéralogie, l'Eau, les Glaces et l'Activité (OMEGA) hyperspectral (~1 to 2.6 μm) imaging observations [*Gendrin et al.*, 2005]. *Arvidson et al.* [2005] and *Griffes et al.* [2007] used 0.4 to 2.5 μm OMEGA data to uncover spectral evidence for kieserite ($Mg^{2+}SO_4$ H_2O, based on overall spectral shape and ~2.1 and 2.4 μm absorptions) in outcrops exposed on the northern walls of a valley that bounds the northern extent of the hematite plains in Meridiani Planum. These authors showed that the absence of Fe^{2+} electronic absorptions associated with another of the kieserite family members (szomolnokite, $Fe^{2+}SO_4$ H_2O) precluded the spectral presence of this mineral. *Griffes et al.* [2007] also identified the presence of polyhydrated sulfate-bearing materials on the valley floor based on the presence of ~1.9 and 2.4 μm absorptions.

CRISM data (~18 m/pixel for FRTs), with the higher spatial resolution as compared to OMEGA observations (hundreds of meters depending on orbital altitude), allowed the identification and mapping of additional hydrated sulfate-bearing outcrop exposures in Meridiani Planum. *Wiseman et al.* [2010] conducted an extensive search using multiple FRTs to detect mineral signatures in and around the hematite-bearing plains and surrounding areas in Meridiani Planum. These authors identified and mapped both kieserite and polyhydrated sulfates, including interbedded units. *Wray* [2011] identified kieserite using FRT data covering the walls and rim rocks of Ada crater using absorptions at ~2.1 and 2.4 μm. *Wray et al.* [2009] used FRT data to infer the presence of polyhydrated sulfates in Burns formation materials around Endeavour crater using the

Table 1. (continued)

FRT000019E9c Botany Bay visited by Opportunity	
Incidence angle	55°
Emergence angle range	20–42°
Phase angle range	30–67°

[a] L_s is the solar longitude or season with $L_s = 0°$ corresponding to the Southern Hemisphere fall equinox. Sol is the Martian solar days after Opportunity's landing. The next four rows correspond to atmospheric optical depths of dust and ice aerosols, CO_2 surface pressure for the central portion of the scenes, and the amount of water vapor that best model the I/F values in DISORT. H_2O ppt stands for the thickness of water that would be precipitated onto the surface if converted from vapor to liquid phases. Detector temperature is provided next. Delta λ is the time-dependent wavelength shift for CRISM observations. The range of elevation, incidence, emergence, and phase angles are then provided for the scene.

presence of absorptions at ~1.94 and 2.4 μm. They also noted the presence of a weak absorption at ~2.2 μm consistent with the presence of an additional hydrated sulfate. *Noe Dobrea et al.* [2012] extended the analysis using several FRTs covering Endeavour crater and surroundings, noting the presence of hydrated Ca sulfates in Burns formation rocks based on the presence of ~1.94, 2.21, and 2.4 μm absorptions.

2.1. Rover Perspective

A number of minerals had been inferred from least squares constrained linear mixing analyses of Opportunity's mast-based Miniature Thermal Emission Spectrometer spectral emission observations of Burns formation materials before the instrument ceased operating. The data were modeled to infer the presence of Mg- and Ca-bearing sulfates and Al-rich opaline silica, in addition to jarosite, plagioclase feldspar, hematite, and perhaps nontronite [*Glotch et al.*, 2006]. Additional information was provided by the arm-based Mössbauer Spectrometer, which was operative until the rover left Santa Maria crater. The 272 day half-life of the ^{57}Co radioactive source precluded use after this period. Mössbauer spectra of Burns formation outcrops show the presence of hematite, jarosite, minor pyroxene, and an unidentified Fe^{3+} phase [*Morris et al.*, 2006]. Both instruments confirmed the presence of hematitic concretions in the Burns formation. Opportunity's remote sensing and in situ measurement capabilities have been used to infer the presence of gypsum in veins cutting the bench surrounding Endeavour's Cape York rim segment [*Squyres et al.*, 2012] and in Cape York rim material proper [*Arvidson et al.*, 2014].

3. Methodology

3.1. CRISM Data Processing and Analysis

Our approach is to use the CRISM ATO data to detect mineralogy in relatively small outcrops (i.e., at the 6 m/pixel scale) and to use Opportunity's ability to traverse across the surface and acquire detailed imaging and in situ measurements of these areas to better understand the geologic and compositional settings associated with the CRISM detections. The discrete ordinates radiative transfer (DISORT) code [*Stamnes et al.*, 1988] was used to model CRISM I/F data (spectral radiance on sensor divided by solar radiance) to retrieve single scattering albedo (SSA) spectra. Atmospheric CO_2, CO, and H_2O gases, together with dust and ice aerosols, were modeled and surface scattering was assumed to follow the Hapke photometric function [*Hapke*, 2012], with a modestly backscattering single-particle phase function. Processing methodology, including the iterative approach used to minimize residual spectral features associated with improperly removed atmospheric gas bands, is discussed in detail in *Arvidson et al.* [2014] and will not be repeated here. The single-particle phase function used is based on the work done by *Fox et al.* [2013] and is typical for surfaces examined by *Johnson et al.* [2006] using Opportunity's Panoramic Camera (Pancam) [*Bell et al.*, 2003].

The advantage of using SSA values is that they are independent of lighting and viewing conditions and only depend on the ensemble of constituent grains and their complex refractive indices, size distribution, and packing, i.e., physically meaningful parameters [*Hapke*, 2012]. The use of DISORT modeling and SSA retrievals negates the need to divide by a "volcano scan" spectrum to remove absorptions associated with atmospheric gases [e.g., *Langevin et al.*, 2005]. In addition, scattering and absorption by dust and ice aerosols are explicitly modeled as part of our processing, unlike the volcano scan approach in which it is assumed that aerosol abundances and size distributions are identical for the data to be processed and the data acquired during the volcano scan. This assumption can lead to errors in identification of subtle absorption features in surface spectra since aerosols scatter and absorb light and can mask these features. This is particularly true for the ~2 to 2.5 μm region, where atmospheric carbon monoxide absorptions not properly modeled with appropriate dust and ice aerosol conditions can interfere with the detection of subtle absorptions associated with

Table 2. Summary of Absorption Features Discussed in Paper[a]

Mineral	Feature (Figure 4)	Center Wavelength (μm)
Kieserite ($MgSO_4 \cdot H_2O$)	K1	1.967 (shoulder)
	K2	2.067
	K3	2.129
	K4	2.399
Gypsum ($CaSO_4 \cdot 2H_2O$)	G1	1.936 and 1.964
	G2	1.980 (shoulder)
	G3	2.178 (shoulder)
	G4	2.218
	G5	2.267
	G6	2.428
	G7	2.476 (shoulder)
Starkeyite ($MgSO_4 \cdot 4H_2O$)	S1	1.940
	S2	1.965 (shoulder)
	S3	2.355 (shoulder)
	S4	2.405
Jarosite (H_3O,Na,K)$Fe^{+3}(SO_4)_2(OH)_6$	J1	1.851
	J2	2.218
	J3	2.265
	J4	2.404
	J5	2.460

[a]Kieserite and gypsum absorptions from *Cloutis et al.* [2006], starkeyite from *Crowley* [1991], and jarosite from *Clark et al.* [1990] and *Cloutis et al.* [2006], in addition to inspection of the laboratory spectra shown in Figure 3. These absorption features are attributed to combination bands variably involving H_2O, OH, together with interactions with Fe and S as detailed by these authors. Letters are keyed to spectra shown in Figures 3 and 4. Shoulder means that the absorption is on the shoulder of a deeper absorption feature. For absorption G1, the 1.936 μm band location is shown on figures used in this paper.

hydrated and hydroxylated mineral phases. *Wiseman et al.* [2014] provide a detailed comparison of volcano scan and DISORT-based retrieval of surface reflectance and summarize limitations of and artifacts produced by the use of volcano scan ratios. The spectral region from 1.0 to 2.65 μm was used in our work because this wavelength interval contains the diagnostic spectral absorption features of interest for hydrated and hydroxylated sulfates relevant to the study area (Table 2).

CRISM is a push-broom imaging spectrometer in which each column of its two-dimensional detector array corresponds to a spectrum in the resulting images [*Murchie et al.*, 2007]. Each row in the detector array corresponds to a particular wavelength of light. For surface targets with high spatial entropy, the rapidly changing brightness patterns relative to the rate of data acquisition and recovery time for detector elements become somewhat problematic and result in spikes when detector element response times are slow. Acquisitions over "busy" scenes can thus be noisy, and extra care is needed to separate signal from noise. Noise spikes in the spectra are easy to identify because they are associated with one to a few CRISM spectral bands, with relatively narrow spectral widths not present in spectra for minerals or outside of wavelengths for which atmospheric gases absorb. Further, CRISM's aging cryogenic coolers are not cooling the detectors to temperatures as low as they did early in the mission (Mars orbit insertion in 2006), making increased dark current noise an additional factor in considering what is signal and what is noise in retrieving SSA spectra.

CRISM data in the wavelength region from ~2.15 to 2.65 μm tend to have the highest signal-to-noise ratio and thus are most reliably interpreted. The reasons are that the onboard integrating sphere lamp's smooth blackbody emission spectrum peaks in this wavelength region, providing a strong signal for calibration purposes. There is also relatively low thermal background from self-emission in the instrument cavity to subtract from the raw data in this wavelength interval. Finally, as shown in Figure 16 of *Murchie et al.* [2007], this wavelength region has the least amount of high-frequency spectral structure in the order sorting filter and thus introduces the least amount of residual "hash" in the calibration to I/F values.

Given the information presented in the previous two paragraphs, particular attention is focused on ensuring that true signal and not noise is being retrieved and interpreted from the CRISM ATO spectra. Further, the spectral region from ~2.15 to 2.65 μm, because of the higher signal to noise relative to shorter wavelengths, is preferentially weighted in the analyses that follow. We adopt a straightforward method for identifying true surface absorptions from noise based on feature band depths. We define band depth (BD) as 1-SSA/SSAc, where SSA is the value at the center of the absorption feature and SSAc is the equivalent value at the same wavelength of the continuum on either side of the absorption feature. Noise BDs are calculated the same way for the same image columns as the mineral-related absorption of interest but above and below the rows for that absorption. The ratio of means for absorption to noise BDs, together with the extent to which absorptions of interest are located in contiguous pixels that have geologically similar contexts, is used as a semiquantitative measure of the confidence with which absorptions can be identified. CRISM I/F data have

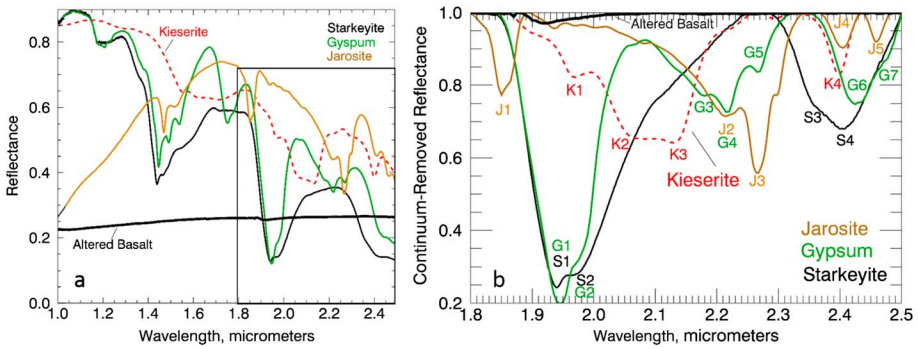

Figure 3. (a) Laboratory spectra are shown for weakly altered basalt rock and powdered kieserite, starkeyite, gypsum, and jarosite. Spectra for gypsum, jarosite, and altered basalt were measured using the Brown University Reflectance Experiment Laboratory facility and are bidirectional spectra from the CRISM spectral library (http://speclib.rsl.wustl.edu/) for samples F1CC16B, F1CC11B, and C1FB03. Kieserite and starkeyite spectra are from *Wang et al.* [2009, 2011] and were acquired with a Nexus 670 FTIR spectrometer fit with a gold-coated rough surface as the reflectance standard. *Wang et al.* [2009, 2011] confirmed their phase identifications using Raman spectroscopy and X-Ray diffraction techniques. Absorption assignments are given in Table 2. (b) Spectra for minerals presented in Figure 3a are shown in continuum-removed form for wavelengths from 1.8 to 2.5 μm. The continuum removal emphasizes absorption features and the wavelength interval used is where numerous features are evident, not well masked by soil, dust, and coatings, and where CRISM has good signal to noise. Key absorption features are labeled and detailed in Table 2.

been heavily processed, including initial radiometric calibrations using preflight and onboard lamps and filtering to suppress noise. It would thus be inappropriate to apply standard statistical tests to infer confidence levels for detection of absorption features. We are developing an end to end procedure, starting from radiometrically calibrated data, and iteratively modeling the signal in the presence of both Poisson and Gaussian noise, but this approach is beyond the scope of our paper.

3.2. Consideration of Absorption Bands

For reference, laboratory reflectance spectra from 1 to 2.5 μm are shown in Figure 3a for representative sulfate minerals: kieserite, starkeyite, gypsum, and jarosite. Continuum-removed values for the spectral range (1.8 to 2.5 μm), with its numerous H_2O, OH, and metal-OH combination absorption features, are shown in Figure 3b. Also shown are values for a slightly altered basaltic rock that is more representative of Mars spectra in amplitude than are the pure powdered spectra shown for the hydrated and hydroxylated sulfate minerals. This sample has Fe^{3+} absorptions in the visible to short-wavelength infrared (not shown), consistent with a minor amount of surface oxidation to produce one or more Fe^{3+}-rich weathering products. A subtle absorption centered at ~1.92 μm is likely associated with adsorbed H_2O or H_2O bound within the Fe^{3+}-rich phase(s). Absorption feature wavelength assignments for each sulfate mineral, based on vibrational modes covering the ~1.8 to 2.5 μm wavelength region (where CRISM can best be used to detect absorptions), are summarized in Table 2. The kieserite spectrum exhibits a suite of major absorptions centered at 2.067, 2.129, and 2.399 μm. Starkeyite ($MgSO_4$ $4H_2O$) is shown to be representative of polyhydrated Mg sulfates and exhibits major absorptions centered at 1.940 and 2.405 μm. As shown by *Crowley* [1991], polyhydrated Mg sulfates are difficult to distinguish from one another using spectra for the wavelength region covered in our paper. The spectrum for gypsum ($CaSO_4$ $2H_2O$) exhibits characteristic multiple major absorptions (e.g., 1.936, 1.964, 2.218, 2.267, and 2.428 μm) that distinguish this mineral from other hydrated sulfates. The spectrum for jarosite $(H_3O,Na,K)Fe^{+3}(SO_4)_2(OH)_6$ shows the hydroxylated but not hydrated nature of this mineral phase. Jarosite exhibits a number of diagnostic OH combination features, as shown in Figure 3 and Table 2. The negative spectral slopes for the hydrated and hydroxylated sulfates are also a characteristic of these minerals for the wavelength interval of interest in our paper and are due to the deep ~3 μm absorption features associated with OH and H_2O vibrations within the mineral structures.

Pure mineral phases such as those shown in Figure 3 have not been identified on Mars for pixel width characteristic of orbital observations, e.g., the hundreds of meters to kilometers for OMEGA [*Bibring et al.*, 2006] or the 18 m/pixel FRT observations. Rather, Opportunity has shown that the sulfate minerals present in the Burns formation materials are intermixed with altered basaltic materials that include hematite and

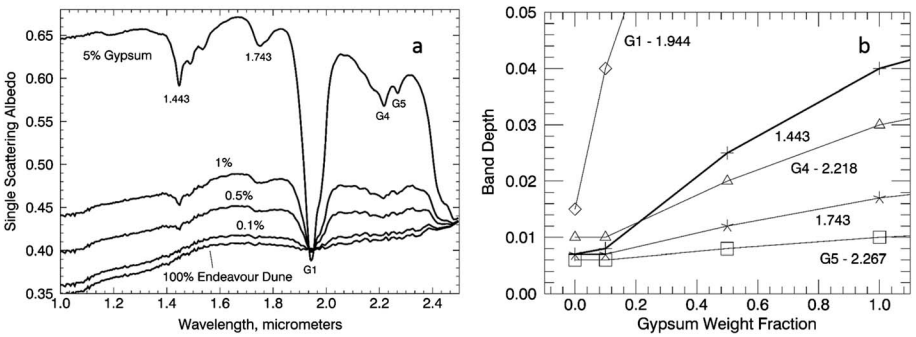

Figure 4. (a) Model SSA spectra are shown for an intimately mixed dune sand end-member (retrieved from ATO FRT00019E9C, location is described in Figure 2) with varying weight percentages of 100 μm diameter gypsum grains. Real and imaginary indices of refraction for gypsum were taken from *Roush et al.* [2007]. Details are provided in the text. Note how the dark dune material subdues the gypsum spectral features, particularly for the shorter wavelengths. (b) Band depths are plotted as a function of weight abundances of gypsum mixed with dune sand for spectra shown in Figure 4a. The band depth values located at 0% gypsum indicate the level of noise in the CRISM spectrum for the dune sand. Note how the shorter-wavelength band depth (bolded line corresponding to 1.443 μm absorption) decreases more rapidly than the longer-wavelength absorption G4 (2.218 μm), consistent with preferentially masking bands at shorter wavelength where the dune sand is darker.

opaline silica [*McLennan et al.*, 2005; *Morris et al.*, 2006; *Arvidson et al.*, 2011]. Further, wind-blown materials dominated by dust and basaltic sands are ubiquitous and can mask the signatures, and coatings can also be present [e.g., *Farrand et al.*, 2007; *Knoll et al.*, 2008]. The combination of dust, soil, coatings, and bedrock properties leads to reflectance spectra for the Meridiani plains that typically increase in amplitude with increasing wavelength from ~1.0 to 2.4 μm [e.g., *Arvidson et al.*, 2006]. In the wavelength region of interest, the optical effects of intermixed grains are nonlinear because multiple scattering is important due to the modest absorption coefficient values. It is also well known that dark materials mask the spectral effects of bright materials when intimately mixed, preferentially subduing the shorter-wavelength spectral features [e.g., *Clark et al.*, 1990].

To illustrate the effects of nonlinear mixing on the appearance and depths of absorption features of interest, we used *Hapke*'s [2012] surface scattering model to provide examples of what happens to spectral features for bright materials when mixed with darker soils. Specifically, *Lapotre et al.* [2014] used *Hapke*'s [2012] nonlinear model to retrieve from SSA spectra (ATO FRT00019E9C; Table 1) the mineral constituents of a barchan dune on the floor of Endeavour crater. They found mineral abundances for hematite, olivine, pigeonite, augite, and labradorite which were, with respect to Fe-bearing minerals, comparable to those found for sands within wind-blown ripples as determined by Opportunity's Mössbauer Spectrometer [*Morris et al.*, 2006]. Starting with this model, numerical simulations were generated by us to show the effect that various weight percentages of 100 μm diameter gypsum grains intimately mixed with these dune sands would have on the resultant SSA spectra. Results are shown in Figure 4 as SSA spectra and BD values for each absorption as a function of weight percent gypsum. Results illustrate how dark materials significantly impact the spectral features of intermixed bright materials, i.e., the 1.443 μm BD decreases with lower abundances of gypsum at a faster rate as compared to the absorption BDs in the 2.0 to 2.5 μm wavelength region. The longer-wavelength absorptions are not attenuated as rapidly because the dune materials are intrinsically brighter in this wavelength interval and allow more multiple scattering. The same result can be reached by coating a gypsum rock with basaltic sand and/or dust with a strong Fe^{3+} oxide or oxyhydroxide component.

4. Ada Crater

Ada is an ~2.2 km diameter crater on the Meridiani plains that is located ~140 km to the east of Endeavour crater and thus will probably not be explored by Opportunity (Figure 1). Even so, the crater is of interest because it is relatively fresh and is covered by CRISM ATO FRT0001FCA1 (Table 1), with a maximum oversampling on the southern side of the crater rim and wall (Figure 5). Regularization of the pixel locations was conducted using a Tikhonov damped least squares approach as discussed in *Arvidson et al.* [2014]. The dispersal of pixels along track evident in the sensor space display shows why regularization

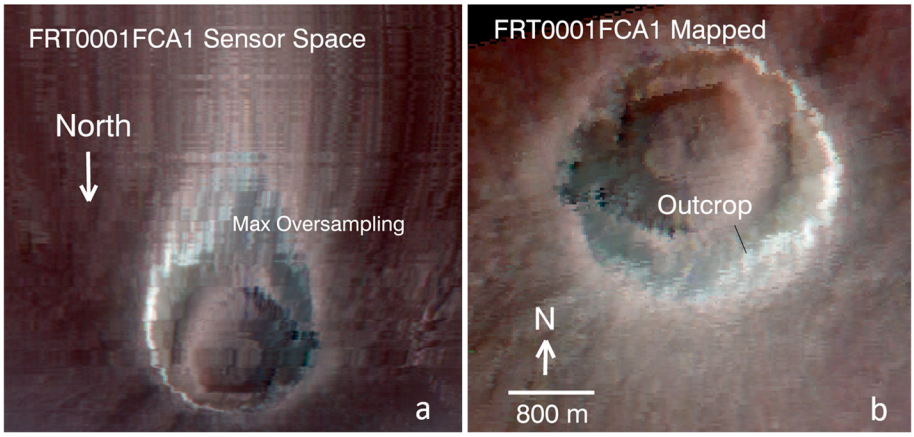

Figure 5. False color infrared view of a portion of ATO FRT0001FCA1 covering the ~2.2 km diameter Ada crater shown in (a) sensor space with oversampling and (b) map projected at 6 m/pixel. Maximum oversampling is associated with the southern portion of the crater rim and wall. Bands located at 1.08, 1.51, and 2.53 μm are shown as blue, green, and red colors (BGR). The spectrum shown in Figure 8 is an average of spectra for the area labeled "outcrop."

is needed. SSA image cubes were generated in sensor space, regularization to 6 m/pixel along track was then conducted, and a map-projected product was produced as the end stage of processing.

HiRISE data covering Ada show exposures of relatively bright bedrock along the rim and upper walls (Figure 6). As part of his PhD thesis, *Wray* [2011] used a normal 18 m/pixel CRISM observation (FRT000199D5) with standard volcano scan processing techniques to infer that the rim and wall outcrops expose kieserite. The ATO and its oversampling of the crater rim and wall are used in this paper to search for the deepest absorption features and to relate these to specific outcrops. The high spatial entropy of Ada's wall and rim outcrops is clearly evident in SSA image cubes for Ada and the scene originally used to detect kieserite. The brightest regions on the rim and upper walls show downward pointing spikes in the retrieved spectra that correspond to the detectors' inability to respond to the rapidly changing dark (narrow valleys not well lit by the Sun and thus dark) to bright surfaces (flatter locations and surfaces tilted toward the Sun) as the instrument field of view moved along track.

A detailed search was conducted to find contiguous spectra with a relatively small number of spikes and deepest absorption features. The retrieved end-member spectra from contiguous pixels are located over a relatively homogeneous outcrop shown at HiRISE spatial resolution in Figure 6, and the resulting average of spectra for 12 pixels is shown in Figure 7a. A plot that allows direct comparisons of the Ada spectrum with laboratory data for kieserite and starkeyite is also shown (Figure 8). Three levels of noise can be identified in

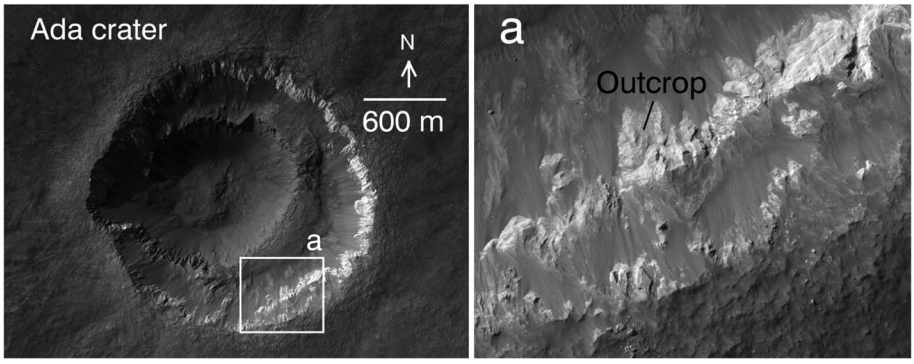

Figure 6. Ada crater is shown in HiRISE views with inset "a" shown at a larger scale. The bright outcrop on the upper wall shows spectral evidence for kieserite, with the deepest bands associated with the outcrop labeled in inset a**.** HiRISE image ESP_018635_1770_red. Illumination is from the upper left.

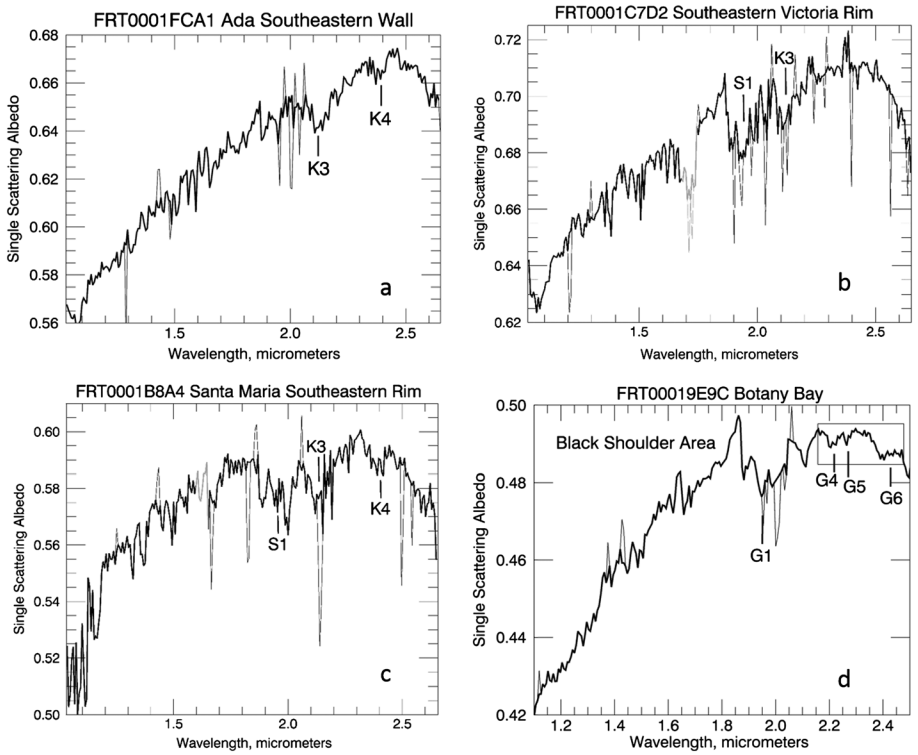

Figure 7. To facilitate comparisons of retrieved CRISM SSA spectra, this figure presents data for Ada, Victoria, Santa Maria, and Botany Bay as a set of four panels. (a) Average of 12 single scattering albedo spectra from FRT0001FCA1 for the outcrop shown in Figure 6. The noisy nature of the CRISM spectrum is a consequence of the small number of spectra being averaged, combined with the rapidly changing pattern of bright and dark areas within Ada relative to the speed of image acquisition, i.e., the inability of the detector elements to fully adapt to the changing conditions. As detailed in the text, the obvious spikes due to lack of proper detector response are shown as light lines. The absorptions K3 and K4 are indicative of kieserite. (b) Single scattering albedo spectra are shown for the southeastern wall of Victoria adjacent to Explorer crater. Spectra for eight pixels were averaged together. Absorption features S1 and K3 are indicative of a hydrated phase and kieserite, respectively. Light portion of the spectrum located at ~1.6 μm is an instrumental artifact as explained in the text. Data from ATO FRT0001C7D2. (c) Single scattering albedo spectra for the southeastern rim of Santa Maria centered on the Luis de Torres in situ target. Six spectra in sensor space were averaged together. The spectra are noisy for the reasons discussed in the text. Absorption features S1, K3, and K4 are indicative of a hydrated phase and kieserite, as discussed in detail in the text. Data from ATO FRT0001B8A4. (d) An average of 400 SSA spectra from ATO FRT00019E9C centered about the Black Shoulder locality. The less noisy nature of the CRISM spectrum relative to those shown for Ada, Victoria, and Santa Maria craters is a consequence of the large number of spectra averaged and the relatively homogeneous spectral characteristics of Botany Bay. The wavelength region from 2.15 to 2.5 μm, delineated by the box, is shown in detail in Figure 17. Absorptions G1, G4, G5, and G6 are indicative of gypsum.

the Ada spectrum. Spikes that clearly deviate from the main spectral trends are due to detector elements that were unable to respond to rapidly changing terrain brightness levels. These spikes have been replaced by averages of the spectrally adjacent values. The ~1.92 to 2.14 μm region includes several deep atmospheric CO_2 bands that cause rapid changes in I/F amplitudes over narrow spectral ranges. As a consequence, this spectral region has not been included in spectral smoothing that is commonly applied to CRISM raw data products [*Murchie et al.*, 2012]. SSA spectra for this spectral region thus tend to have high noise levels. The typical noise level standard deviation is evident through examination of the spectrum shown in Figure 7a. As noted previously, the spectral region from ~2.15 to 2.65 μm tends to have lower noise values as compared to shorter-wavelength data.

Absorptions consistent with K3 (2.129 μm) and K4 (2.399 μm) are evident in the Ada spectrum and consistent with kieserite (Table 3). The downturn at longest wavelengths is also consistent with the presence of hydrated sulfates, including kieserite. The absorption present in kieserite spectra centered at ~1.6 μm (Figure 3) is not evident in the spectrum shown for Ada. This is interpreted to be due to the higher opacity of basaltic soil and/or

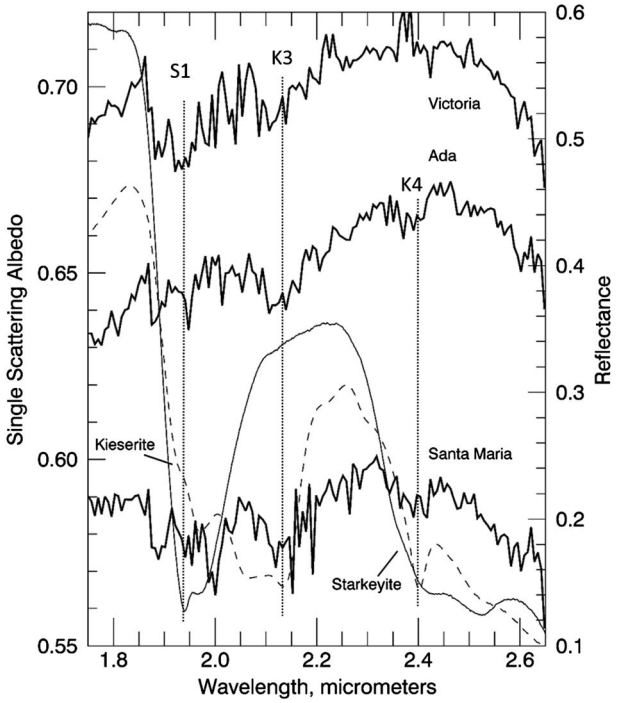

Figure 8. To allow direct comparisons of SSA spectra for Ada, Victoria, and Santa Maria, areas for which kieserite detections have been inferred, the data are shown on one plot (without obvious data spikes), along with laboratory spectra for pure samples of kieserite and starkeyite. Absorption features (S1, K3, and K4) are labeled. The laboratory data have been scaled to fit onto the SSA range for CRISM-derived spectra. The different shapes for the two sets of spectra are a consequence of using pure powders for the laboratory data and mixtures of materials with relatively low concentrations of kieserite and polyhydrated sulfate(s) for Mars. The lack of refractive index data for kieserite and starkeyite precluded nonlinear calculations of the type used in Figure 4 to show simulated spectra for low concentrations of gypsum mixed with basaltic materials that dominate Mars.

dust in this wavelength region, the low expected BD value based on the shallow-longer-wavelength bands, and the high level of noise in this wavelength region. We have also considered the possibility that the spectra are indicative of the presence of szomolnokite ($Fe^{2+}SO_4 H_2O$), given that absorption features are similar to those for kieserite in the spectral region considered. We note that this mineral was not found for any Burns formation targets examined by Opportunity using the Mössbauer Spectrometer, which is sensitive to the presence of Fe-bearing minerals (*Morris et al.* [2006] and later data collected for Burns formation rocks). Szomolnokite cannot be excluded based on Ada spectra, although given the lack of detections for other Burns formation locations, we prefer a kieserite interpretation, an interpretation shared by *Wray* [2011].

It is beyond the scope of this paper to estimate the relative amount, grain size distribution, and porosity of the kieserite-bearing outcrops, parameters that are needed to simulate multiple scattering of light in soil deposits using either *Hapke*'s [2012] or *Shkuratov et al.*'s [1999] models. The important point is that what we interpret to be kieserite spectrally dominates the outcrops exposed on the rim and walls of Ada. These rocks are located near the top of the preserved Burns formation stratigraphic section based on the fact that the crater did not penetrate into the Noachian substrate; i.e., there is no spectral or morphologic evidence for excavation of basaltic Noachian crust. Based on the nonlinear mixing model example shown in Figure 4, the inferred kieserite abundance need not be more than a few percent, although lower or higher values are permissible, given that the mixing model is for particulate matter and not rock. Pure or relatively pure outcrops of kieserite are excluded based on the spectrum shown in Figure 7a and the data Opportunity collected to the west of Ada for Burns formation outcrops.

5. Victoria Crater

Victoria crater formed after the deposition of the Burns formation and has since undergone significant wind-induced erosion of its rim [*Grant et al.*, 2008; *Squyres et al.*, 2009]. Opportunity explored the plains to the northwest and north of the rim and spent its second Martian winter within the crater, systematically investigating an ~8 m vertical section of Burns formation sulfate-rich sandstones exposed on Victoria's walls [*Squyres et al.*, 2009]. Examination of ATO FRT0001C7D2 SSA spectra in sensor space and in map-projected formats illustrates the need to regularize the pixel locations to true map locations (Figure 9). In particular, pixels on the southern rim were oversampled in an irregular way. Oversampling is densest along the southeastern rim. Processing was done using the methodologies described in previous sections of this paper.

SSA image cube data in sensor space regularized to 6 m/pixel show spectra with varying degrees of downward and upward spikes, particularly in areas where HiRISE data show irregular topography along the

Table 3. Band Depths (BDs) Calculated for Absorptions Identified From CRISM ATO Data[a]

Absorption	Absorption BD	Noise BD	Absorption BD/Noise BD
		Ada Crater	
K3	0.025	0.011	2.3
K4	0.017	0.011	1.6
		Victoria Crater	
S1	0.040	0.020	2.0
K3	0.029	0.015	1.9
		Santa Maria Crater	
S1	0.030	0.010	3.0
K3	0.030	0.015	2.0
K4	0.022	0.015	1.5
		Botany Bay, Endeavour Crater	
G1	0.040	0.010	4.0
G4	0.008	0.004	2.0
G5	0.006	0.004	1.5
G6	0.010	0.003	3.3

[a]Noise BDs were calculated for image rows above and below the rows with absorption features of interest. For reference, BDs calculated from laboratory data shown in Figure 3 have BD values that are an order of magnitude or more greater than those calculated for ATO data. BD ratios less than 1.5 were discounted in our analyses.

dissected rim and thus large changes in lighting conditions over short distances. The spectral signatures with the deepest absorptions (Figure 7b) are associated with an outcrop on the southeastern rim, just to the northwest of the ~40 m wide Explorer crater (Figure 10). A significant number of downward spikes are present in the average spectrum of 8 pixels retrieved from this area and are interpreted to reflect the lag of some detector elements in responding to the higher radiances from bright rim materials. In addition, another artifact common to some CRISM spectra appears, centered at ~1.7 μm, that is associated with the boundary between two order filters [*Murchie et al.*, 2007]. The spikes and the artifact are shown as lighter lines, with the spike values replaced by averages of spectrally adjacent SSA values. Two absorptions are evident in the spectrum and are indicative of what we interpret to be kieserite (K3, 2.129 μm) and one or more hydrated phases (S1, 1.940 μm). The 2.4 μm spectral region shows as a column-dependent, noise-induced plateau above the continuum. This unfortunate situation precludes detection of a kieserite-related narrow

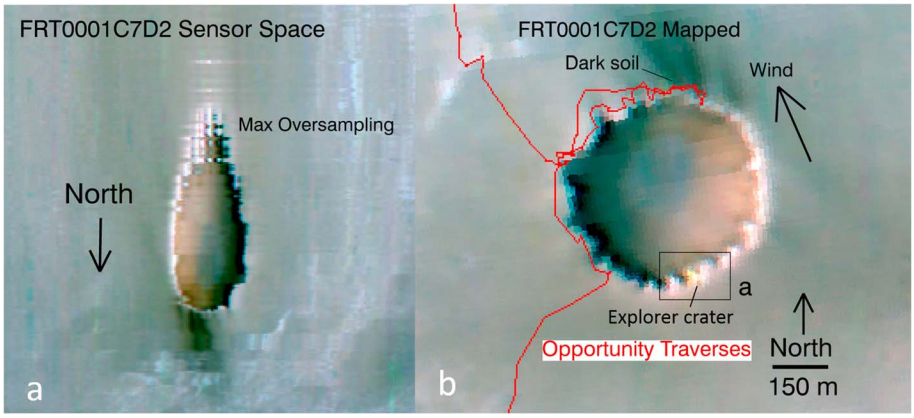

Figure 9. False color infrared view of a portion of ATO FRT0001C7D2 covering the ~800 m diameter Victoria crater shown in (a) sensor space with oversampling and (b) map projected at 8 m/pixel and overlain with Opportunity's traverses. Location delineated by box a is where relatively deep absorption features are evident as shown in Figure 7b. A HiRISE view of this area is shown in Figure 10. Spectra retrieved from this location show a distinctive kieserite signature likely due to wind erosion of overlying soils exposing a relatively clean bedrock surface. Bands located at 1.08, 1.51 and 2.53 μm are shown as BGR.

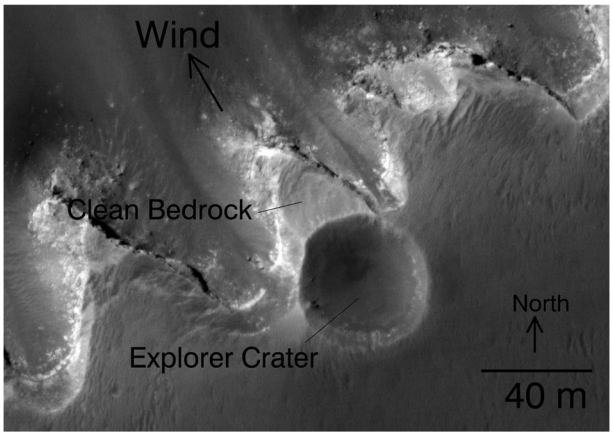

Figure 10. Portion of a HiRISE frame showing an ~40 m wide crater (Explorer) located immediately to the southeast of Victoria's wall. Southeasterly winds moving around Explorer caused scour of a small portion of Victoria's rim and wall, exposing relatively clean bedrock with a kieserite spectral signature (Figure 7b). HiRISE frame ESP_016644_1780_red. Illumination from the upper left.

absorption or the broader feature associated with polyhydrated sulfates. The downturn at the longest wavelengths is also consistent with the presence of hydrated sulfates. The lack of the ~1.6 μm kieserite absorption is again attributed to the reduction of spectral contrast by admixed dark soil, expected shallow band depths, and high noise levels at these shorter wavelengths.

HiRISE data show that the area with the kieserite detection is relatively bright and stripped of soil by southeasterly winds (Figure 10). A portion of the Pancam false color Cape Verde mosaic (Jet Propulsion Laboratory Photojournal PIA090103), taken from the northwestern Victoria rim, shows the location with the CRISM detection of kieserite, including Explorer crater (Figure 11). Dark sands can be seen extending down the walls and into the crater. This is consistent with the direction of dark wind-blown sands extending to the northwest from Victoria and sampled by Opportunity to show the presence of basaltic materials [*Geissler et al.*, 2010]. Thus, we infer that southeasterly winds have preferentially removed dust, soil, and any coatings and exposed relatively fresh bedrock, enabling detection of what we infer to be kieserite and an additional hydrated phase. We note that Opportunity did acquire remote sensing and contact science measurements for outcrops on the northwestern side of Victoria crater. Mössbauer Spectrometer observations for these outcrops preclude the presence of szomolnokite. Rather, the data are indicative of the presence of the typical Burns formation Fe-rich phases: hematite, jarosite, minor pyroxene, and an unidentified Fe^{3+} phase. Kieserite is thus inferred to be at the top of the locally preserved Burns formation stratigraphic section.

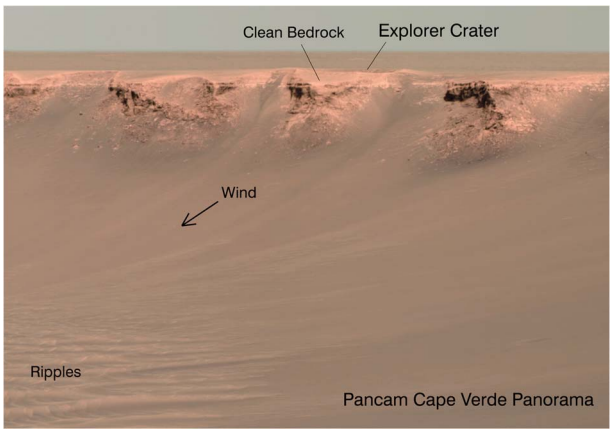

Figure 11. Pancam false color view from Cape Verde of the southeastern portion of Victoria's rim and walls for the region that shows the kieserite signature. Explorer crater is labeled. Images were acquired on sols 970 to 991. Note the dark sands extending into the crater walls and floor from the rim. This view is a portion of the Cape Verde panorama acquired from the northwestern side of Victoria. Pancam bands L2, L5, and L7 (0.753, 0.535, and 0.432 μm) are shown as BGR.

6. Santa Maria Crater

CRISM ATO FRT0001B8A4 was acquired over the ~100 m wide Santa Maria crater and surroundings, while Opportunity was still on its way from Victoria to Endeavour craters. Initial results from the analyses of this data set showed the presence of what we interpret to be kieserite and were used to help define the location on the rim of Santa Maria for Opportunity to acquire in situ and remote sensing measurements. HiRISE data show that Santa Maria is relatively fresh and has exposures of the preserved upper section of the Burns formation (Figure 12). ATO-regularized sensor space data converted to SSA values were carefully searched to find the best evidence for absorption features. Results show that the southeastern rim of the crater has spectra for 6 pixels consistent with the presence of absorptions K3 (2.129 μm) and K4 (2.399 μm), with the

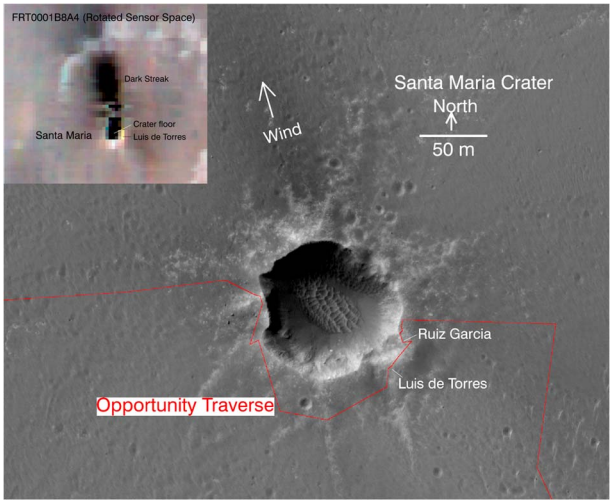

Figure 12. Portion of a HiRISE view of the relatively fresh Santa Maria crater with Opportunity traverses shown in red and the inset on upper left showing a portion of CRISM ATO FRT0001B8A4 in sensor space (rotated 180°). Note the bright crater rim and dark soil extending outward to the northwest. Luis de Torres and Ruiz Garcia are two targets for which Opportunity acquired in situ measurements. HiRISE frame PSP_009141_1780_red. CRISM bands located at 1.08, 1.51, and 2.53 μm shown as BGR, respectively, for the ATO image in the upper left. Illumination from the upper left.

addition of S1 (1.940 μm) (Figure 7c). The spectra for this portion of the rim are interpreted to be indicative of kieserite, with the addition of another hydrated phase. The downturn at the longest wavelengths is also consistent with the presence of hydrated sulfates.

Opportunity spent a solar conjunction period on the southeastern portion of Santa Maria's rim where the CRISM spectra shown in Figures 7c and 8 were retrieved. Opportunity conducted detailed in situ measurements of the rock target Luis de Torres (Figures 13 and 14) and another rock target called Ruiz Garcia. Mössbauer Spectrometer observations preclude the presence of szomolnokite and instead are indicative of the presence of the typical Fe-rich phases for Burns formation outcrops: hematite, jarosite, minor pyroxene, and an unidentified Fe^{3+} phase. Pancam observations from this site show that dark sands are located within the crater and piled up against the northwestern wall and rim (Figure 13). ATO data show that dark sands extend to the northwest away from the crater (Figure 12). The location of the kieserite and hydrated phase spectral signatures on the southeastern side of the rim is thus consistent with preferential scouring of the site by southeasterly winds, similar to what was found for Victoria; i.e., wind-scoured surfaces at the top of the preserved Burns formation stratigraphic section show evidence for kieserite. A partial dust and soil cover are evident even in these scoured locations, based on Microscopic Imager (MI) [*Herkenhoff et al.*, 2003] images of the brushed Luis de Torres target (Figure 14). Loose dust and soil were brushed away by the Rock Abrasion Tool and can be seen at the periphery of the circular brushed zone. This cover would preferentially mask shorter-wavelength absorptions, as noted in a previous section of our paper.

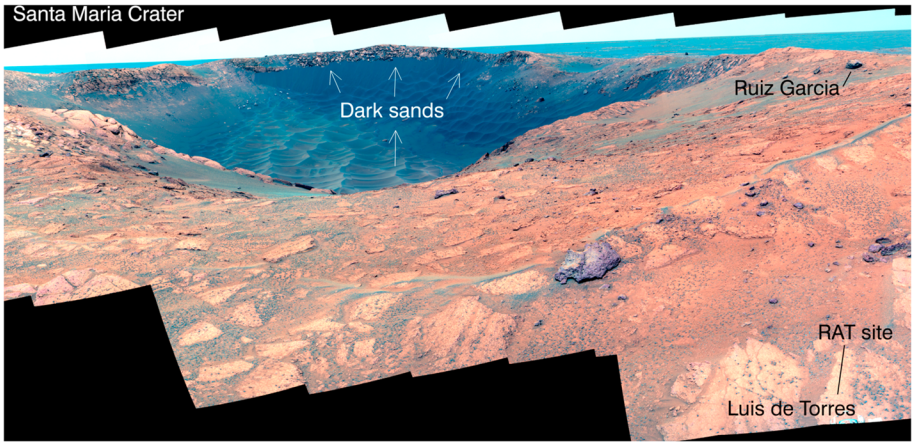

Figure 13. Pancam false color mosaic looking northwest into Santa Maria crater acquired from the Luis de Torres in situ target area on the southeastern rim of the crater. Note the dark sands extending up onto the northwestern wall of the crater. Images were acquired on sols 2512 to 2517. Pancam bands L2, L5, and L7 (0.753, 0.535, and 0.432 μm) are color composited as BGR. The Luis de Torres Rock Abrasion Tool (RAT) target is shown, along with the in situ boulder target Ruiz Garcia.

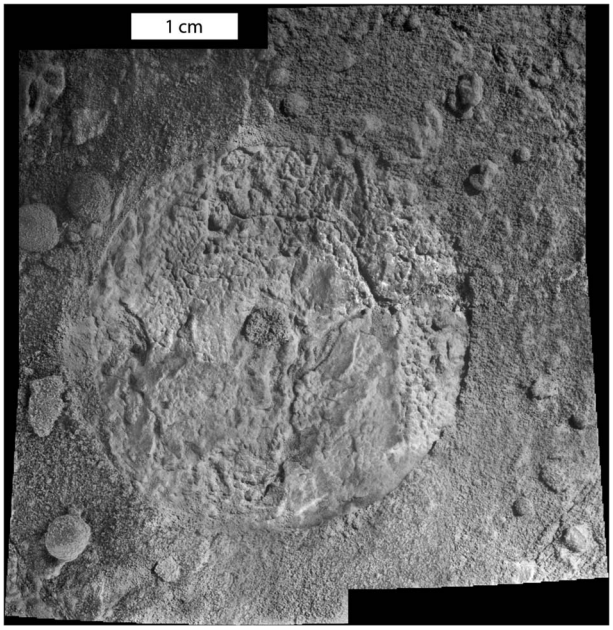

Figure 14. Microscopic Imager mosaic of Luis de Torres after brushing using the RAT on sol 2485 and processed to minimize effects of partial shadows. Brushed area is ~3.8 cm wide. Hematitic concretions common on the Meridiani plains can be seen around the brushed area. Surface materials were removed during the 34 min brushing period and can be seen as fine materials exterior to the brushed region.

7. Botany Bay on Endeavour Crater's Rim

A key objective for Opportunity has been the exploration of the rim of the ~22 km diameter, Noachian age Endeavour crater [*Squyres et al.*, 2012; *Arvidson et al.*, 2014]. After exploring Endeavour's Cape York rim segment, Opportunity was commanded to traverse across Botany Bay, a subdued portion of the rim covered by Burns formation materials (Figure 15). This area has a higher thermal inertia relative to surrounding terrains, suggesting that loose, fine-grained material has been preferentially removed from this area (Figure 16). In fact, *Chojnacki et al.* [2011] showed, using mesoscale atmospheric circulation models, that winds tend to move up and out of Endeavour, making Botany Bay a wind gap with enhanced erosion. *Noe Dobrea et al.* [2012] used FRT data to show that Botany Bay has a spectral signature of hydrated Ca sulfates. To follow up on this discovery, ATO FRT00019E9C (Table 1) was acquired and processed, and the resulting SSA cube was searched for the locations with the strongest absorption signatures to help determine where to send Opportunity to characterize the relevant outcrops and more fully characterize the mineralogy associated with the hydrated Ca sulfate signatures.

A BD map centered at 1.936 μm (G1; Table 2) was generated and used both to retrieve spectra with deepest absorption features and to direct Opportunity to a location to explore the surface materials associated with this signature (Figure 16). The 1.936 μm BD map correlates well with the thermal inertia map (Figure 16), consistent with the hypothesis that wind has scoured soil and exposed more bedrock than typical for Burns formation outcrops. Detailed examination of the ATO SSA image cube showed spectra consistent with the presence of G1, G4, G5, and G6 absorptions for gypsum, with the strongest signatures present on a broad area on the southern side of Botany Bay where both thermal inertia and the 1.936 μm BD map showed high values. An average of 400 spectra centered about this strong signature is shown in Figures 7d and 17. The data are also consistent with a minor amount of an additional polyhydrated sulfate phase, such as starkeyite, with its 1.940 (S1) and broad 2.405 μm (S4) absorptions. The presence of bassanite ($2CaSO_4{\cdot}H_2O$, with absorptions centered at 1.912, 2.094, 2.252, and 2.474 μm [*Crowley*, 1991]) is not consistent with the data; in that, the deep absorption at 1.912 μm is not evident, the absorption located at 2.094 μm is in the spectral regime with a relatively high noise level for identification of this feature, and there is no evidence for an absorption at 2.252 nor 2.474 μm.

Opportunity was directed to the southeastern side of Botany Bay where CRISM data indicated a strong gypsum spectral signature (Figures 16; Black Shoulder). The terrain consists of relatively bright, flat-lying outcrops, partially covered by basaltic sand, and a field of slightly darker, upturned boulders that is interpreted to be the remains of a resistant layer left behind as Burns formation rocks were eroded by wind (Figure 18). Detailed in situ observations were obtained for an ~0.6 m wide, upturned boulder called Black Shoulder (Figure 19). MI data for Black Shoulder show a coarse-grained rock with little to no soil cover in which the interlocking nature of the grains is indicative of extensive aqueous alteration after deposition [e.g., *Grotzinger et al.*, 2005]. Black Shoulder Alpha Particle X-Ray Spectrometer (APXS) [*Rieder et al.*, 2003] measurements do not show enhancement of Ca and S indicative of the presence of a Ca sulfate, as will be detailed in the next section of this paper.

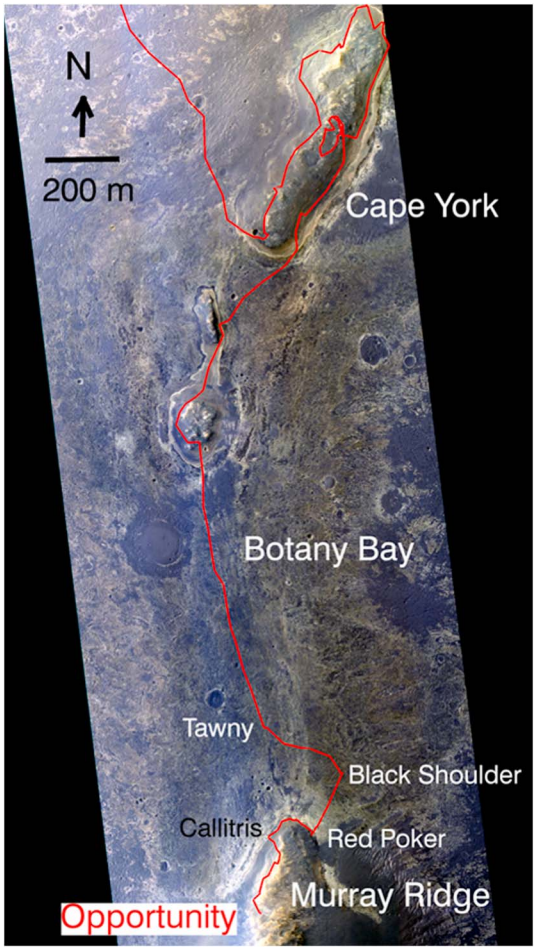

Figure 15. Shown is a false color HiRISE image view of the Botany Bay area overlain with Opportunity's traverses from the Meridiani plains to Murray Ridge. Tawny, Black Shoulder, Red Poker, and Callitris are in situ targets on Burns formation materials. The Black Shoulder target included brushing and abrading with the RAT. Opportunity was directed to the Black Shoulder area based on a strong CRISM detection of gypsum in that locality (Figures 7d and 17). HiRISE frame ESP_033573_1775_color with illumination from the upper left. Composite generated using 0.40–0.60, 0.55–0.85, and 0.80–1.00 μm bands as BGR.

MI and APXS data were also acquired in Botany Bay for the flat-lying bedrock outcrops Tawny, Red Poker, and Callitris (Figure 16). The Callitris target was the last Burns formation in situ measurement site before ascending onto Murray Ridge (Figures 20 and 21). The Callitris outcrop lies stratigraphically above the older bench materials (so-called Grasberg outcrops) that surround the ridge, and APXS data show slight enhancement of Ca and S, consistent with the presence of a Ca sulfate. This evidence will be presented in the next section of this paper. It is noted that veins interpreted to contain gypsum have been found by Opportunity on the bench materials surrounding Cape York, deposits that drape unconformably onto the rim materials [*Rice et al.*, 2010; *Squyres et al.*, 2012]. Similar veins were found on rim materials on Cape York proper [*Arvidson et al.*, 2014]. The evidence is in the form of APXS data for veins that show enhanced Ca and S, together with Pancam spectra that show a distinct ~1.0 μm downturn uniquely associated with an H_2O and/or OH combination absorption for gypsum.

8. Correspondence Analysis Applied to Burns Formation APXS Data

Although Opportunity did not visit the southeastern rim area of Victoria crater where CRISM spectra indicate the presence of kieserite, in situ measurements were made as a function of stratigraphic position within the walls on the northwestern side of this crater. Thus, an extensive set of measurements exist for the crater. Also, the Luis de Torres in situ target for Santa Maria crater was located in the center of the kieserite-rich signature as observed in the ATO FRT0001B8A4 data. Furthermore, several flat-lying bedrock and the Black Shoulder boulder in situ targets in Botany Bay were in areas with gypsum signatures. In this section of the paper, we explore the extent to which compositional information derived from APXS measurements is consistent with inferences from the spectral information derived from the CRISM ATOs. Table 4 provides the compositional data used in the analysis.

APXS data are multivariate in nature (oxide compositions for any number of targets) with variations in any given oxide controlled by dependencies on other oxides. Correspondence analysis (CA) is a normalized factor analysis in which factor loadings are generated for both variables and samples and has been validated for use in compositional data sets [e.g., *Larsen et al.*, 2000]. When shown as scatterplots of factor loadings, APXS observations for Opportunity have been used to show contributions from admixed soils (trends from soil covered to brushed to abraded surfaces), along with trends of increasing iron oxide concentrations near the crests of granule ripples on the Meridiani plains [*Arvidson et al.*, 2011].

CA was applied to all APXS measurements acquired on Burns formation surfaces from Victoria through the last measurement (Callitris) before Opportunity traversed onto the Noachian-aged rocks on Murray Ridge

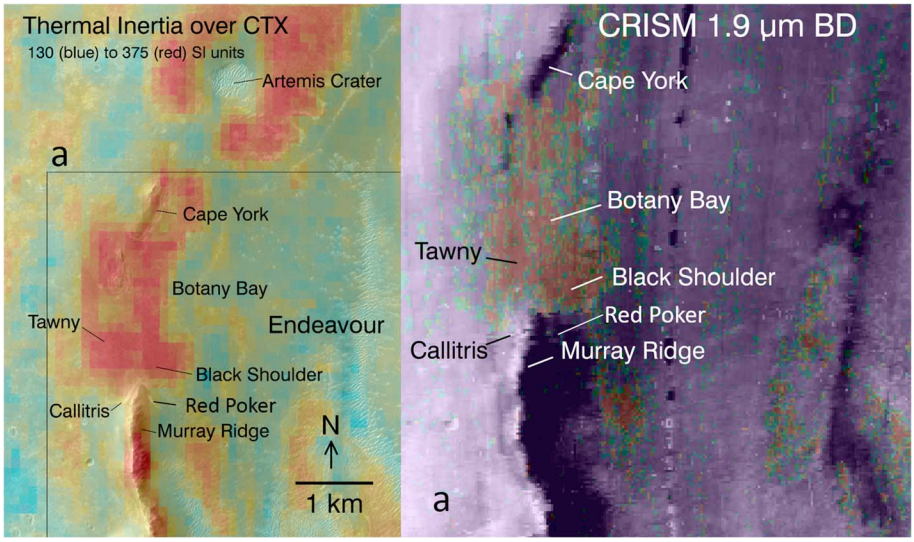

Figure 16. Color-coded thermal inertia values superimposed onto an MRO Context Imager mosaic centered over Botany Bay on Endeavour's rim. Note the enhanced thermal inertia over Botany Bay, which is inferred to be due to preferential wind erosion that keeps the area relatively clean of fine-grained soils. Thermal inertia values based on analysis of THEMIS data as reported in *Putzig et al.* [2005]. Box a delineates the location for which a portion of ATO FRT00019E9C in false color infrared is overlain with a color-coded 1.944 μm band depth map, showing values larger than 0.015 (blue) up to 0.021 (red). Opportunity was directed to Tawny and the Black Shoulder areas based on high thermal inertia and band depth values. CRISM bands located at 1.08, 1.51, and 2.53 μm shown as BGR. Note that Callitris is just at the edge of enhanced thermal inertia and band depth values whereas Red Poker is located to the south of these enhanced areas.

(Figure 16). For reference, data for a dust-dominated surface (North Pole) measured on a ripple located on the northern part of Cape York were also included (Table 4). The factor 1 loading from a correspondence analysis for these data accounts for 88% of the data set variance and is controlled by the extent of dust and soil cover, and any coatings, with a trend from undisturbed to brushed to abraded rock targets becoming increasingly enriched in S (Figure 22). For example, the undisturbed Luis de Torres target at Santa Maria crater exhibits an extreme factor 1 loading for Burns formation targets, with affinities associated with silicates that dominate soil and dust. The North Pole measurement is the extreme end-member, consistent with significant dust and soil covers (dominated by silicates and ferric oxides) for the undisturbed Burns formation surfaces. The factor 1 loadings are also consistent with MI data that show at least partial removal of wind-blown dust and soil covers after brushing the Luis de Torres target (e.g., Figure 14); in that, the loading after brushing lies in an intermediate location between undisturbed and abraded target loadings. The abraded target lies on the other extreme for factor 1 loading. Ruiz Garcia is a boulder target at Santa Maria crater, with a near-vertical face (likely minimal dust and soil cover), and has a factor 1 loading similar to the brushed target for Luis de Torres. Similar trends from undisturbed to abraded surface measurements are evident for targets in Victoria and Botany Bay.

Factor 2 loading (Figure 22) explains about 5% of the variance. The sample locations show an increased spread in the second factor loading from measurements on undisturbed to brushed to abraded surfaces, consistent with systematically removing contaminants to reveal the subtle variations in rock compositions. Tawny and Callitris are flat-lying targets in Botany Bay, and these measurements represent outliers slightly enriched (see Table 4) in Ca, in addition to enhanced thermal inertias and 1.936 μm band depth values. These are in areas where CRISM data indicate the dominance spectrally of gypsum. The enrichments are relatively small (Table 4), consistent with the relatively shallow band depths inferred from CRISM spectra. For the remaining targets, there is no clear positive correlation between S and other elements, implying that the system was to first order isochemical, with the exception of an increase in Cl downsection for the measurements within Victoria. The downsection movement of Cl is interpreted to be a consequence of movement of soluble salts by percolating groundwaters after deposition of the Burns formation [*Arvidson et al.*, 2011]. The lack of a correlation between Ca and S extends to the Black Shoulder rock target in Botany Bay, which as discussed in the paper is likely an outlier left behind as wind erosion stripped the Burns formation.

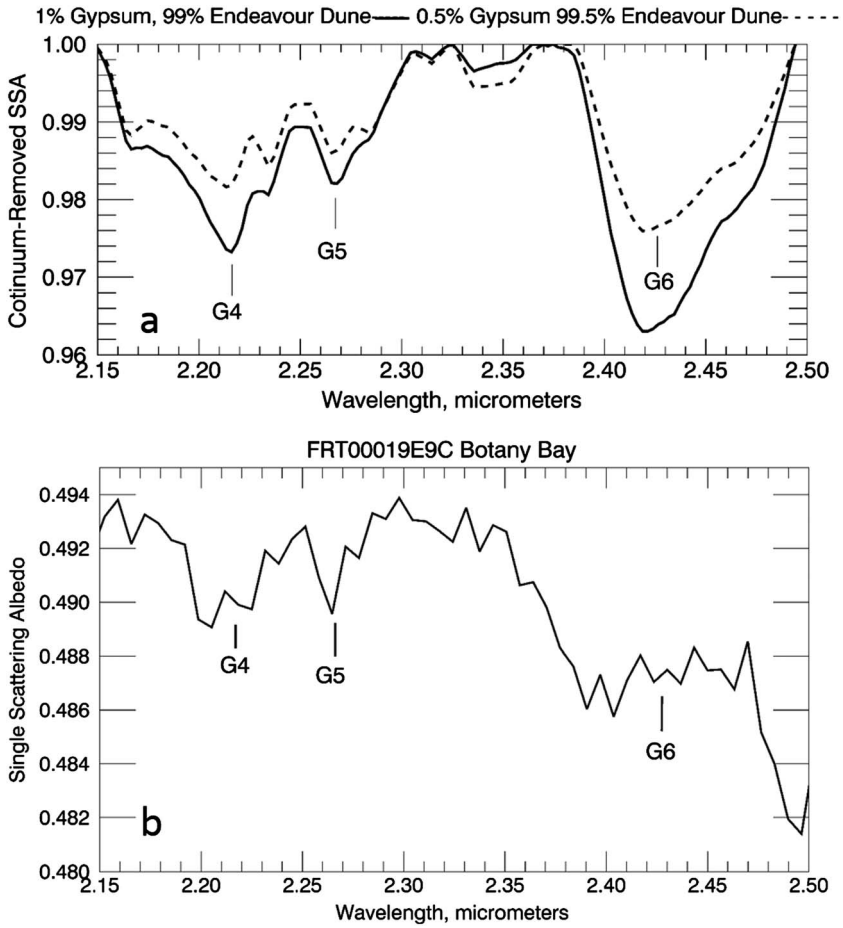

Figure 17. (a) Continuum-removed spectra for 1% and 0.5% by weight of gypsum intimately mixed with dune sands (from data shown in Figure 4). (b) Enlarged view of Botany Bay spectrum shown in Figure 7d showing absorptions G4, G5, and G6 indicative of gypsum.

9. Implications for Formation and Alteration of the Burns Formation

Both kieserite and gypsum, where encountered in bedrock exposures on Mars, tend to be relatively resistant to erosion. For example, the gypsum-bearing veins explored by Opportunity are local high areas, standing above the more eroded bench rocks surrounding Endeavour's rim [*Squyres et al.*, 2012]. As another example, *Griffes et al.* [2007] showed that kieserite bordering the northern Meridiani Plains is associated with plateau-forming strata. It thus seems reasonable that the enhanced exposures of these two minerals as evidenced by ATO-based signatures for wind-swept rock exposures (or crater walls for Ada) may be due to differential erosion relative to weaker materials, perhaps polyhydrated sulfates and perhaps jarosite. In any case, the identification of kieserite and gypsum still provides constraints on the deposition and/or alteration of Burns formation materials, as summarized below.

Deposition of the Burns formation has been ascribed to a fundamental change in the hydrologic environment of the Meridiani area, from one dominated by fluvial erosion and transport of material to the northwest along the topographic gradient [*Hynek and Phillips*, 2001] to accumulation of sulfate-rich, predominantly wind-blown sedimentary deposits [*Grotzinger et al.*, 2005]. Recharge from the highlands located to the southeast of Meridiani would have provided the necessary hydrostatic head for groundwater to preferentially reach the surface in the Meridiani area [*Andrews-Hanna et al.*, 2010].

Edgar et al. [2014] infer that a sulfate-bearing mudstone facies has been preserved in rocks exposed in Santa Maria crater, whereas in other areas explored by Opportunity (e.g., Victoria), the sedimentary deposits likely resulted from reworking of putative playa muds by wind and water into a "wetting upward" sequence

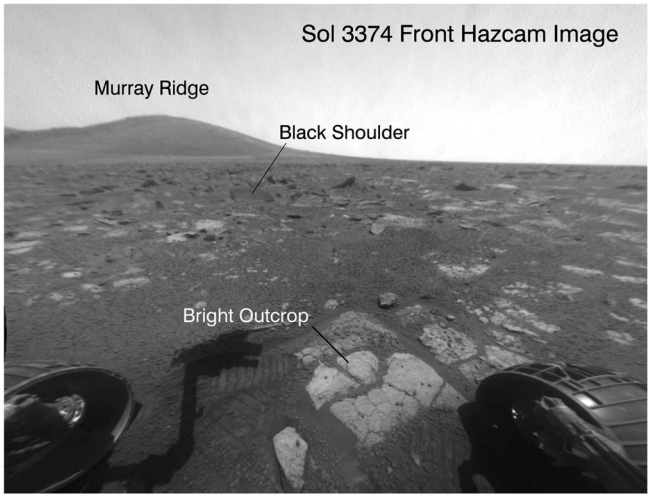

Figure 18. Front Hazcam image of the ~0.6 m wide boulder Black Shoulder acquired on sol 3374 in Botany Bay. Black Shoulder was the subject of a detailed MI and APXS measurement campaign with the target shown by the line extending from the label Black Shoulder. View is to the south with Murray Ridge in the background. Note the finely layered boulders that are strewn across Botany Bay. Sand and granule-sized grains are evident near the two front wheels. Frame 1F427716180RSLC6DHP1214R0MZ.

of sulfate-rich wind-blown sandstones (sand grains are composed of sulfate-cemented, altered basaltic mud) [*Grotzinger et al.*, 2005; *McLennan et al.*, 2005; *Squyres et al.*, 2009]. The oxidizing and acidic conditions that have been inferred for the formation of the sulfate-rich Burns formation materials could have been a consequence of rising anoxic groundwater, carrying cations and anions associated with corrosion of subsurface basalt into contact with an oxidizing atmosphere. This would have led to oxidation of dissolved Fe^{2+}, with consequent lowering of aqueous pH, further corrosion of near-surface basaltic material and subsequent deposition of playa muds, formation of sulfate-rich cements within the sandstones, and one or more diagenetic episodes resulting in the formation of hematitic concretions and jarosite [*Hurowitz et al.*, 2010].

Two topics to be addressed from the results reported in this paper are why gypsum is preferentially found in Botany Bay and surroundings and why kieserite is preferentially found on outcrops in Ada, Victoria, and Santa Maria craters (i.e., closer to the top of the preserved Burns formation stratigraphic section). We address the gypsum question first. For materials of basaltic composition, the neutralization of sulfate-rich acidic groundwaters that are expected to result from fluid-rock interaction would produce Mg-Fe-Ca-Na-SO_4-rich

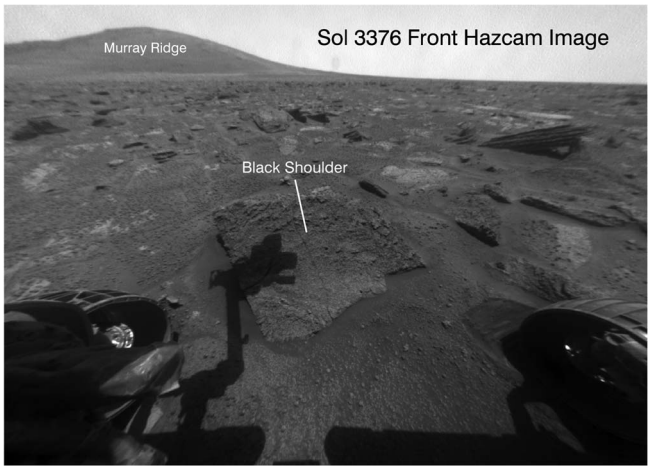

Figure 19. Front Hazcam image showing the rock Black Shoulder in among a field of boulders sitting on flat-lying outcrops. Line points to location for which MI and APXS data were acquired. Frame 1F427893692RSLC6E2P1214L0MZ.

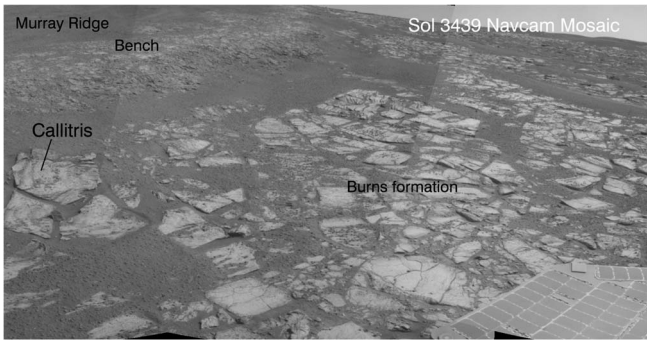

Figure 20. Navcam mosaic acquired looking to the east and south from the Meridiani plains to the bench that surrounds Murray Ridge. The western flank of Murray Ridge is also evident in the scene. Callitris was the target for MI and APXS measurements for the Burns formation rock exposure located stratigraphically above the bench materials. The width of the Callitris outcrop is approximately 0.60 m.

fluid(s) that upon rising to the surface and undergoing evaporation would generate a specific sequence of sulfate minerals [*Tosca and McLennan*, 2009]. Gypsum would form and deplete the fluid of Ca and S well before the onset of polyhydrated sulfate precipitation, which only occurs after evaporation further concentrates the fluid [*Tosca and McLennan*, 2009]. In addition, polyhydrated sulfates and chlorides, precipitated from late-stage brines, are far more likely to undergo complex redissolution and reprecipitation processes during any recharge of subsequent groundwaters, potentially leading to further preferential concentration of less soluble gypsum [*McLennan*, 2012].

The presence of gypsum in Botany Bay is thus interpreted to be a consequence of its proximity to the underlying Noachian crust, with initial rising of groundwaters preferentially precipitating gypsum as a relatively insoluble phase [*Tosca and McLennan*, 2009]. This may have happened in locations more proximal to fertile groundwater sources, while the Burns formation was being emplaced and/or afterwards as the Burns formation materials were diagenetically altered by subsequent groundwater recharge events. The

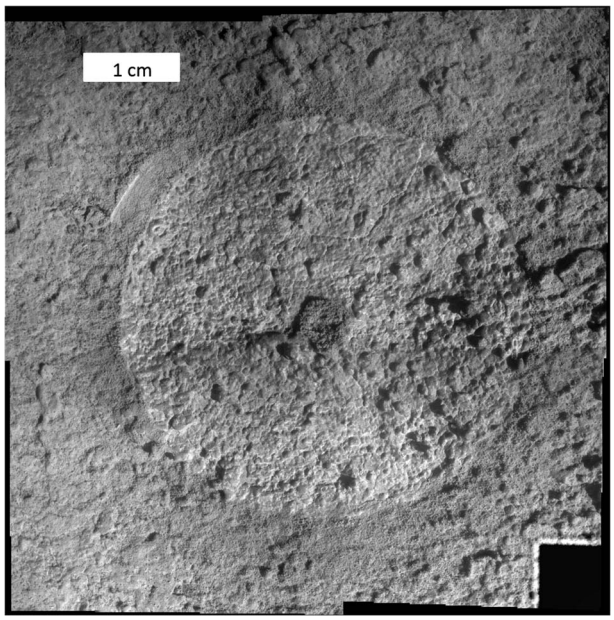

Figure 21. MI mosaic of the brushed Callitris target acquired on sol 3343 showing the clastic nature of the rock with numerous rounded sand grains. Illumination is from the lower right. Mosaic covers ~5 cm in width. Product ID 1380666395_23879-1_mi_mosaic.jpg.

Table 4. APXS Compositional Data for Burns Formation Targets in Victoria Crater to Botany Bay[a]

	Na_2O	MgO	Al_2O_3	SiO_2	P_2O_5	SO_3	Cl	K_2O	CaO	MnO	FeO
Average statistics error (%)	15	3	2	2	10	2	4	10	2	10	2
Approximate accuracy (%)	15	15	7	4	15	15	30	15	7	10	10
NorthPole2	2.38	7.14	8.83	44.3	0.94	7.80	0.91	0.52	6.72	0.37	18.6
Steno	1.88	7.51	7.00	39.4	1.03	18.36	0.87	0.54	5.26	0.29	16.7
Steno_Brush	1.63	7.40	6.04	36.3	1.01	23.22	0.80	0.49	5.35	0.31	16.4
Steno_Abraded	1.46	7.23	5.32	34.4	1.00	26.38	0.68	0.52	5.62	0.33	16.1
Hall	2.05	7.21	7.33	40.0	1.02	17.20	0.89	0.53	5.44	0.32	16.9
Smith	2.16	7.47	8.11	42.5	1.01	12.72	0.98	0.52	6.17	0.26	16.8
SmithBrushed	1.71	7.65	5.84	36.1	1.07	23.24	0.81	0.58	4.34	0.29	17.2
SmithBrushed2	1.70	7.63	5.85	36.1	1.04	23.21	0.78	0.57	4.37	0.26	17.2
Smith2	2.09	7.18	8.17	42.8	0.99	11.79	0.96	0.55	6.31	0.32	17.5
Smith2_Abraded	1.70	7.27	6.10	37.2	1.03	22.02	0.84	0.58	4.47	0.29	17.3
Lyell1_asis	2.00	7.53	7.13	39.2	1.03	17.96	1.11	0.55	5.49	0.26	16.5
Lyell1_Abraded	1.47	7.82	5.80	35.7	1.04	23.41	1.43	0.58	4.28	0.29	17.0
Lyell2	2.13	7.31	7.60	40.7	1.03	15.59	1.10	0.57	5.76	0.28	16.7
Lyell	2.07	7.36	7.54	40.8	1.02	15.79	1.12	0.55	5.64	0.27	16.6
Smith3	1.93	7.42	7.30	39.9	1.05	16.69	1.08	0.56	5.75	0.32	16.8
Smith3	1.99	7.36	7.37	40.0	1.01	16.67	1.07	0.56	5.71	0.35	16.7
Lyell4	2.03	7.45	7.25	39.6	1.04	17.29	1.15	0.56	5.51	0.33	16.6
Lyell4	2.01	7.41	7.18	39.6	1.02	17.45	1.14	0.56	5.46	0.32	16.7
Ly33ell4	2.01	7.40	7.29	39.5	1.00	17.32	1.16	0.57	5.55	0.33	16.7
Lyell5	2.12	7.24	7.86	41.6	0.99	13.81	1.02	0.54	6.08	0.34	17.2
Lyell5	2.17	7.30	7.95	41.6	1.02	13.65	1.02	0.54	6.01	0.36	17.2
Lyell_Buckland	2.15	7.30	7.77	40.9	1.00	14.58	1.07	0.53	6.30	0.37	16.8
Lyell_Buckland_Abraded	1.60	7.49	5.64	35.1	0.99	22.95	1.70	0.55	4.71	0.36	17.8
Lyell_Exeter	2.09	7.13	7.92	41.6	0.96	13.49	1.12	0.53	6.36	0.33	17.2
Lyell_Exeter	2.16	7.22	8.01	41.4	1.00	13.48	1.10	0.55	6.33	0.34	17.2
Gilbert	2.14	7.24	8.42	43.3	0.96	10.50	1.04	0.51	6.65	0.37	17.6
Gilbert_Abraded	1.94	5.99	6.68	40.7	1.07	17.38	1.41	0.63	4.46	0.34	18.2
LuisDeTorres	2.35	7.30	8.60	43.6	1.00	9.61	0.90	0.53	6.41	0.32	18.0
LuisDeTorres	2.28	7.28	8.60	43.5	0.97	9.72	0.88	0.51	6.42	0.35	18.1
LuisDeTorres_Brush	1.86	7.14	6.89	39.3	1.04	19.11	0.82	0.54	5.72	0.30	16.2
LuisDeTorres_Abraded	1.67	7.89	5.81	36.1	1.06	23.79	0.54	0.59	4.63	0.32	16.4
RuizGarcia	1.83	7.18	6.60	38.6	1.03	20.36	1.27	0.61	5.02	0.29	16.0
Valdivia	2.04	7.56	7.31	40.2	1.03	16.92	1.09	0.56	5.22	0.28	16.7
Gibraltar	2.13	7.41	7.77	41.8	1.03	13.70	1.01	0.57	6.19	0.30	16.9
Tawny	1.83	6.80	7.58	40.7	0.96	11.93	0.81	0.54	6.54	0.27	20.9
BlackShoulder	1.81	8.35	6.81	38.4	1.03	19.72	1.18	0.60	4.66	0.25	16.0
BlackShoulder2	1.79	7.73	7.16	39.3	1.03	17.65	1.17	0.55	5.59	0.30	16.5
BlackShoulder3	1.96	7.96	6.69	37.6	1.00	19.86	1.40	0.53	6.00	0.21	15.6
BlackShoulder_Abraded	1.78	8.15	5.95	36.5	1.02	22.36	1.60	0.64	4.28	0.23	16.5
RedPoker	2.07	7.14	7.50	40.6	1.04	15.53	1.05	0.57	6.16	0.29	16.8
Callitris_Brush	1.54	5.52	6.71	39.4	1.06	18.77	0.84	0.49	7.46	0.15	16.9

[a]Eleven element oxide compositions in weight percent were used in the correspondence analysis discussed in the paper and presented as factor loadings in Figure 22. Trace elements were not utilized. The average statistical error bars for each element, representing the statistical uncertainty for each measured spot, are given in the table. The average accuracy values for the MER APXS calibration found in the laboratory with homogeneous powdered geological reference samples are also given [*Gellert et al.*, 2006]. Brushing and abrasion were done using the Athena Rock Abrasion Tool [*Squyres et al.*, 2004].

lack of gypsum veins based on Opportunity data for the Burns formation suggests that gypsum formation was dispersed through Burns formation materials (e.g., as cements or altered grains).

With regard to kieserite, laboratory experiments indicate that this phase does not form as a direct low-temperature evaporative precipitate [*Vaniman et al.*, 2004], unless there is a large amount of chlorine present, and an extensive assemblage of chlorides would then accompany kieserite deposition [*Vaniman et al.*, 2004; *Wang*, 2014]. On the other hand, chloride salts are approximately 3 times more soluble than Mg sulfates [*Arvidson et al.*, 2010] and might not survive any redissolution processes that may have taken place. Kieserite thus may have formed during last stages of evaporation of brines. It may also have formed as a

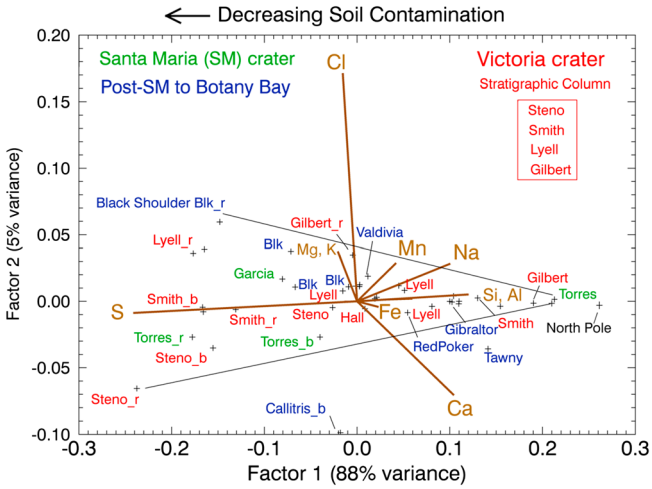

Figure 22. Results for correspondence analysis (CA) of Opportunity's APXS observations (expressed as oxide weight percentages, see Table 4 for data) of Burns formation materials from Victoria through Botany Bay are shown as a scatterplot for the first two factor loadings. CA allows exploration of multidimensional data sets by retrieving the most important directions of data variance in a way that allows factor loadings for both samples, and variables to be plotted together. For clarity, phosphorus is not labeled but is aligned with the sulfur vector. See *Arvidson et al.* [2011] for detailed description and application to Opportunity APXS data for Endurance and Victoria craters. Key samples are labeled with (right) undisturbed surfaces, (middle) brushed surfaces ("b"), and (left) abraded surfaces ("r"). This is consistent with a greater degree of dust and soil contamination for natural as opposed to abraded surfaces, with the North Pole dust measurement lying on the extreme right of the factor 1 loading. For Victoria, (top to bottom) the stratigraphic sections are Steno, Smith, Lyell, and Gilbert. The lines extending from the undisturbed Luis de Torres data to abraded Black Shoulder and Steno measurements encompass most of the data and show how subtle rock compositional trends become evident after removal of dust and soil covers and any coatings. Tawny and Callitris data from Botany Bay lie outside of the trend and toward an enhancement in Ca.

dehydration product of polyhydrated sulfates that precipitated in a chemically complex evaporative sequence. For example, kieserite has been inferred to be present on the surfaces of newly exposed epsomite deposits on the dry, cold Tibetan Plateau on Earth [*Kong et al.*, 2014]. The kinetics of the dehydration and hydration of sulfates under Mars conditions are complex and sluggish, and implications for the presence of outcrops on Mars dominated by polyhydrated as opposed to monohydrated sulfates are still under investigation in laboratory experiments [*Chipera and Vaniman*, 2007; *Steiger et al.*, 2011; *Wang*, 2014]. We hypothesize that for either direct precipitation or dehydration scenarios, the occurrence of kieserite at the top of the preserved Burns formation stratigraphic section implies that this mineral formed during latter stages of deposition when conditions moved toward aridity.

Acknowledgments

We thank the capable team of engineers and scientists at the Jet Propulsion Laboratory and elsewhere who made the Opportunity mission possible, together with the project personnel and scientists associated with the Mars Reconnaissance Orbiter and Mars Odyssey Missions. A particular thank you is extended to the CRISM Science Operations Center personnel at the Applied Physics Laboratory (APL), Johns Hopkins University. This work was supported in part by contracts to Washington University in Saint Louis from APL and Cornell University. Data are available from the NASA Planetary Data System (https://pds.jpl.nasa.gov/).

References

Andrews-Hanna, J. C., M. T. Zuber, R. E. Arvidson, and S. J. Wiseman (2010), Early Mars hydrology: Meridiani playa deposits and the sedimentary record of Arabia Terra, *J. Geophys. Res.*, *115*, E06002, doi:10.1029/2009JE003485.

Arvidson, R. E., F. Poulet, J.-P. Bibring, M. Wolff, A. Gendrin, R. V. Morris, J. J. Freeman, Y. Langevin, N. Mangold, and G. Bellucci (2005), Spectral reflectance and morphologic correlations in eastern Terra Meridiani, Mars, *Science*, *307*(5715), 1591–1594, doi:10.1126/science.1109509.

Arvidson, R. E., et al. (2006), Nature and origin of the hematite-bearing plains of Terra Meridiani based on analyses of orbital and Mars Exploration rover data sets, *J. Geophys. Res.*, *111*, E12S08, doi:10.1029/2006JE002728.

Arvidson, R. E., et al. (2010), Spirit Mars Rover Mission: Overview and selected results from the northern Home Plate Winter Haven to the side of Scamander crater, *J. Geophys. Res.*, *115*, E00F03, doi:10.1029/2010JE003633.

Arvidson, R. E., et al. (2011), Opportunity Mars Rover mission: Overview and selected result from Purgatory ripple to traverses to Endeavour crater, *J. Geophys. Res.*, *116*, E00F15, doi:10.1029/2010JE003746.

Arvidson, R. E., et al. (2014), Ancient aqueous environments at Endeavour Crater, Mars, *Science*, *343*(6169), doi:10.1126/science.1248097.

Bell, J. F., III, et al. (2003), The Mars Exploration Rover Athena Panoramic Camera (Pancam) investigation, *J. Geophys. Res.*, *108*(E12), 8063, doi:10.1029/2003JE002070.

Bibring, J.-P., Y. Langevin, J. F. Mustard, F. Poulet, R. Arvidson, A. Gendrin, B. Gondet, N. Mangold, P. Pinet, and F. Forget (2006), Global mineralogical and aqueous Mars history derived from OMEGA/Mars Express data, *Science*, *312*, 400–404, doi:10.1126/science.1122659.

Chipera, S. J., and D. T. Vaniman (2007), Experimental stability of magnesium sulphate hydrates that may be present on Mars, *Geochim. Cosmochim. Acta*, *71*, 241–250.

Chojnacki, M., D. M. Burr, J. E. Moersch, and T. I. Michaels (2011), Orbital observations of contemporary dune activity in Endeavour crater, Meridiani Planum, Mars, *J. Geophys. Res.*, *116*, E00F19, doi:10.1029/2010JE003675.

Clark, R. N., T. V. V. King, M. Klejwa, and G. A. Swayze (1990), High spectral resolution reflectance spectroscopy of minerals, *J. Geophys. Res.*, *95*, 12,653–12,680, doi:10.1029/JB095iB08p12653.
Cloutis, E. A., et al. (2006), Detection and discrimination of sulfate minerals using reflectance spectroscopy, *Icarus*, *184*, 121–157, doi:10.1016/j.icarus.2006.04.003.
Crowley, J. K. (1991), Visible and near-infrared (0.4–2.5 μm) reflectance spectra of playa evaporate minerals, *J. Geophys. Res.*, *96*, 16,231–16,240, doi:10.1029/91JB01714.
Edgar, L. A., J. P. Grotzinger, J. F. Bell III, and J. A. Hurowitz (2014), Hypotheses for the origin of fine-grained sedimentary rocks at Santa Maria crater, Meridiani Planum, *Icarus*, *234*, 36–44, doi:10.1016/j.icarus.2014.02.019.
Farrand, W. H., et al. (2007), Visible and near infrared multispectral analysis of in situ and displaced rocks, Meridiani Planum, Mars by the Mars Exploration Rover Opportunity: Spectral properties and stratigraphy, *J. Geophys. Res.*, *112*, E06S02, doi:10.1029/2006JE002773.
Fox, V. K., R. E. Arvidson, and M. J. Wolff (2013), Quantifying surface scattering parameters for bright and dark Martian surfaces, Abstract P23F-1861 presented at Fall Meeting, AGU, San Francisco, Calif., 9–13 Dec.
Fraeman, A. A., et al. (2013), A hematite-bearing layer in Gale Crater, Mars: Mapping and implications for past aqueous conditions, *Geology*, *41*, 1103–1106, doi:10.1130/G34613.1.
Geissler, P. E., R. Sullivan, M. Golombek, J. R. Johnson, K. Herkenhoff, N. Bridges, A. Vaughan, J. Maki, T. Parker, and J. Bell (2010), Gone with the wind: Eolian erasure of the Mars rover tracks, *J. Geophys. Res.*, *115*, E00F11, doi:10.1029/2010JE003674.
Gellert, R., et al. (2006), Alpha Particle X-Ray Spectrometer (APXS): Results from Gusev crater and calibration report, *J. Geophys. Res.*, *111*, E02S05, doi:10.1029/2005JE002555.
Gendrin, A., et al. (2005), Sulfates in martian layered terrains: The OMEGA/Mars Express view, *Science*, *307*(5715), 1587–1591, doi:10.1126/science.1109509.
Glotch, T. D., J. L. Bandfield, P. R. Christensen, W. M. Calvin, S. M. McLennan, B. C. Clark, A. D. Rogers, and S. W. Squyres (2006), Mineralogy of the light-toned outcrop rock at Meridiani Planum as seen by the Miniature Thermal Emission Spectrometer and implications for its formation, *J. Geophys. Res.*, *111*, E12S03, doi:10.1029/2005JE002672.
Grant, J. A., S. A. Wilson, B. A. Cohen, M. P. Golombek, P. E. Geissler, R. J. Sullivan, R. L. Kirk, and T. J. Parker (2008), Degradation of Victoria crater, Mars, *J. Geophys. Res.*, *113*, E11010, doi:10.1029/2008JE003155.
Griffes, J. L., R. E. Arvidson, F. Poulet, and A. Gendrin (2007), Geologic and spectral mapping of etched terrain deposits in northern Meridiani Planum, *J. Geophys. Res.*, *112*, E08S09, doi:10.1029/2006JE002811.
Grotzinger, J. P., et al. (2005), Stratigraphy and sedimentology of a dry to wet eolian depositional system, Burns formation, Meridiani Planum, Mars, *Earth Planet. Sci. Lett.*, *240*, 11–72, doi:10.1016/j.epsl.2005.09.039.
Hapke, B. (2012), *Theory of Reflectance and Emittance Spectroscopy*, Cambridge Univ. Press, New York.
Herkenhoff, K. E., et al. (2003), The Athena Microscopic Imager investigation, *J. Geophys. Res.*, *108*(E12), 8065, doi:10.1029/2003JE002076.
Hurowitz, J. A., W. W. Fischer, N. J. Tosca, and R. E. Milliken (2010), Origin of acidic surface waters and the evolution of atmospheric chemistry on early Mars, *Nat. Geosci.*, *3*, 323–326, doi:10.1038/ngeo831.
Hynek, B. M., and R. J. Phillips (2001), Evidence for extensive denudation of the martian highlands, *Geology*, *29*, 407–410.
Johnson, J. R., et al. (2006), Spectrophotometric properties of materials observed by Pancam on the Mars Exploration Rovers: 2. Opportunity, *J. Geophys. Res.*, *111*, E12S16, doi:10.1029/2006JE002762.
Knoll, A. H., et al. (2008), Veneers, rinds, and fracture fills: Relatively late alteration of sedimentary rocks at Meridiani Planum, Mars, *J. Geophys. Res.*, *113*, E06S16, doi:10.1029/2007JE002949.
Kong, W. G., M. P. Zheng, F. J. Kong, and W. X. Chen (2014), Sulfate-bearing deposits at Dalangtan Playa and their implication for the formation and preservation of martian salts, *Am. Mineral.*, *99*, 283–290, doi:10.2138/am.2014.4594.
Langevin, Y., F. Poulet, J. P. Bibring, and B. Gondet (2005), Sulfates in the North Polar region of Mars, *Science*, *307*, 1584–1586, doi:10.1126/science.1109091.
Lapotre, M. G. A., B. L. Ehlmann, and R. E. Arvidson (2014), Quantitative composition, granulometry of aeolian bedforms in Endeavour and Gale Craters inferred from visible near-infrared spectra, Abstract 1431 presented at the 45th Lunar and Planetary Science Conference, The Woodlands, Tex., 17–21 March.
Larsen, K. W., R. E. Arvidson, B. L. Jolliff, and B. C. Clark (2000), Correspondence and least squares analyses of soil and rock compositions for the Viking Lander 1 and Pathfinder landing sites, *J. Geophys. Res.*, *105*, 29,207–29,221, doi:10.1029/2000JE001245.
McEwen, A. S., et al. (2007), Mars Reconnaissance Orbiter's High Resolution Imaging Science Experiment (HiRISE), *J. Geophys. Res.*, *112*, E05S02, doi:10.1029/2005JE002605.
McLennan, S. M. (2012), Geochemistry of sedimentary processes on Mars, in *Sedimentary Geology of Mars*, *Spec. Publ.*, vol. 102, edited by J. P. Grotzinger and R. E. Milliken, pp. 119–138, SEPM, Tulsa, Okla.
McLennan, S. M., et al. (2005), Provenance and diagenesis of sedimentary rocks in the vicinity of the Opportunity landing site, Meridiani Planum, Mars, *Earth Planet. Sci. Lett.*, *240*, 95–121, doi:10.1016/j.epsl.2005.09.041.
Morris, R. V., et al. (2006), Mössbauer mineralogy of rock, soil, and dust at Meridiani Planum, Mars: Opportunity's journey across sulfate-rich outcrop, basaltic sand, dust, and hematite lag deposits, *J. Geophys. Res.*, *111*, E12S15, doi:10.1029/2006JE002791.
Murchie, S. L., et al. (2007), CRISM (Compact Reconnaissance Imaging Spectrometer for Mars) on MRO (Mars Reconnaissance Orbiter), *J. Geophys. Res.*, *112*, E05S03, doi:10.1029/2006JE002682.
Murchie, S. L., E. A. Guinness, and S. Slavney (2012), CRISM Data Products Software Interface Specification Document, v. 1.3.7.1. [Available at http://pds-geosciences.wustl.edu/mro/mro-m-crism-2-edr-v1/mrocr_0001/document/crism_dpsis.pdf.]
Noe Dobrea, E. Z., J. J. Wray, F. J. Calaf III, T. J. Parker, and S. L. Murchie (2012), Hydrated minerals on Endeavour Crater's rim, interior, and surrounding plains: New insights from CRISM data, *Geophys. Res. Lett.*, *39*, L23201, doi:10.1029/2012GL053180.
Putzig, N. E., M. Mellon, K. Kretke, and R. E. Arvidson (2005), Global thermal inertia, and surface properties of Mars from the MGS Mapping Mission, *Icarus*, *173*, 325–341, doi:10.1016/j.icarus.2004.08.017.
Rice, M. S., J. F. Bell III, E. A. Cloutis, A. Wang, S. Ruff, M. A. Craig, D. T. Bailey, J. R. Johnson, P. A. de Souza Jr., and W. H. Farrand (2010), Silica-rich deposits and hydrated minerals at Gusev Crater, Mars: Vis-NIR spectral characterization and regional mapping, *Icarus*, *205*, 375–395, doi:10.1016/j.icarus.2009.03.035.
Rieder, R., R. Gellert, J. Brückner, G. Klingelhöfer, G. Dreibus, A. Yen, and S. W. Squyres (2003), The new Athena alpha particle X-ray spectrometer for the Mars Exploration Rovers, *J. Geophys. Res.*, *108*(E12), 8066, doi:10.1029/2003JE002150.
Roush, T. L., F. Esposito, G. R. Rossman, and L. Colangeli (2007), Estimated optical constants of gypsum in the regions of weak absorptions: Application of scattering theories and comparisons to independent measurements, *J. Geophys. Res.*, *112*, E10003, doi:10.1029/2007JE002920.
Shkuratov, Y., L. Starukhina, H. Hoffmann, and G. Arnold (1999), A model of spectral albedo of particulate surfaces: Implications for optical properties of the Moon, *Icarus*, *137*, 235–246.

Squyres, S. W., et al. (2004), The Opportunity Rover's Athena Science Investigation at Meridiani Planum, Mars, *Science*, *306*(5702), 1698–1703, doi:10.1126/science.1106171.

Squyres, S. W., et al. (2009), Exploration of Victoria crater by the Mars Rover Opportunity, *Science*, *324*, 1058–1061, doi:10.1126/science.1170355.

Squyres, S. W., et al. (2012), Ancient impact and aqueous processes at Endeavour Crater, Mars, *Science*, *336*, 570–576, doi:10.1126/science.1220476.

Stamnes, K., S. C. Tsay, W. Wiscombe, and K. Jayaweera (1988), Numerically stable algorithm for discrete-ordinate-method radiative transfer in multiple scattering and emitting layered media, *Appl. Opt.*, *27*, 2502–2509, doi:10.1364/AO.27.002502.

Steiger, M., K. Linnow, D. Ehrhardt, and M. Rohde (2011), Decomposition reactions of magnesium sulfate hydrates and phase equilibria in the $MgSO_4$-H_2O and Na^+-Mg^{2+}-C^{l-}-SO_4^{2-}-H_2O systems with implications for Mars, *Geochim. Cosmochim. Acta*, *75*(12), 3600–3626.

Tosca, N. J., and S. M. McLennan (2009), Experimental constraints on the evaporation of partially oxidized acid-sulfate waters at the Martian surface, *Geochim. Cosmochim. Acta*, *73*, 1205–1222.

Vaniman, D. T., D. L. Bish, S. J. Chipera, C. I. Fialips, J. W. Carey, and W. C. Feldman (2004), Magnesium sulphate salts and the history of water on Mars, *Nature*, *431*, 663–665.

Wang, A. (2014), Nature, formation and climatic meaning of interbedded sulfate stratigraphy on Mars, Abstract 1058 presented at the 8th International Conference on Mars, USRA, Pasadena, Calif., 14–18 July.

Wang, A., J. F. Freeman, and B. L. Jolliff (2009), Phase transition pathways of the hydrates of magnesium sulfate in the temperature range 50°C to 5°C: Implication for sulfates on Mars, *J. Geophys. Res.*, *114*, E04010, doi:10.1029/2008JE003266.

Wang, A., J. J. Freeman, I.-M. Chou, and B. L. Jolliff (2011), Stability of Mg-sulfates at −10° C and the rates of dehydration/rehydration processes under conditions relevant to Mars, *J. Geophys. Res.*, *116*, E12006, doi:10.1029/2011JE003818.

Wiseman, S. M., R. E. Arvidson, R. V. Morris, F. Poulet, S. L. Murchie, F. P. Seelos, J. L. Bishop, J. C. Andrews-Hanna, D. Des Marais, and J. L. Griffes (2010), Spectral and stratigraphic mapping of hydrated sulfate and phyllosilicate-bearing deposits in northern Sinus Meridiani, Mars, *J. Geophys. Res.*, *115*, E00D18, doi:10.1029/2009JE003354.

Wiseman, S. M., et al. (2014), Characterization of artifacts introduced by the empirical volcano-scan atmospheric correction commonly applied to CRISM and OMEGA near-infrared spectra, *Icarus*, doi:10.1016/j.icarus.2014.10.012.

Wray, J. J. (2011), High-resolution studies of aqueous environments on ancient Mars, PhD thesis, Cornell Univ., Ithaca, N. Y.

Wray, J. J., E. Z. Noe Dobrea, R. E. Arvidson, S. M. Wiseman, S. W. Squyres, A. S. McEwen, J. F. Mustard, and S. L. Murchie (2009), Phyllosilicates and sulfates at Endeavour Crater, Meridiani Planum, Mars, *Geophys. Res. Lett.*, *36*, L21201, doi:10.1029/2009GL040734.